2017

Gravitational Potential Modeling of Near-Earth Contact Binaries

Stephanie Wood
University of Vermont

Recommended Citation

Wood, Stephanie, "Gravitational Potential Modeling of Near-Earth Contact Binaries" (2017). *Graduate College Dissertations and Theses*. 753.
https://scholarworks.uvm.edu/graddis/753

GRAVITATIONAL POTENTIAL MODELING OF NEAR-EARTH CONTACT BINARIES

A Thesis Presented

by

Stephanie Wood

to

The Faculty of the Graduate College

of

The University of Vermont

In Partial Fullfillment of the Requirements
for the Degree of Master of Science
Specializing in Mechanical Engineering

May, 2017

Date: March 20, 2017
Thesis Examination Committee:

Darren Hitt, Ph.D., Advisor
James Bagrow, Ph.D., Chairperson
Chris Danforth, Ph.D., Chairperson
Dryver Huston, Ph.D.
Cynthia J. Forehand, Ph.D., Dean of the Graduate College

Abstract

A significant component of recent space exploration has been unmanned mission to comets and asteroids. The increase in interest for these bodies necessitates an increase in demand for higher fidelity trajectory simulations in order to assure mission success. Most available methods for simulating trajectories about asymmetric bodies assume they are of uniform density. This thesis examines a hybrid method that merges a mass concentration ("mascon") model and a spherical harmonic model using the "Brillouin sphere" as the interface. This joint model will be used for simulating trajectories about variable density bodies and, in particular, contact binary asteroids and comets.

The scope of this thesis is confined to the analysis and characterization of the spherical harmonic modeling method in which three bodies of increasing asymmetrical severity are used as test cases: Earth, asteroid 101955 Bennu, and asteroid 25143 Itokawa. Since the zonal harmonics are well defined for Earth, it is used as the initial baseline for the method. Trajectories in the equatorial plane and inclined to this plane are simulated to analyze the dynamical behavior of the environment around each of the three bodies. There are multiple degrees of freedom in the spherical harmonic modeling method which are characterized as follows: (1) The radius of the Brillouin sphere is varied as a function of the altitude of the simulated orbit, (2) The truncation degree of the series is chosen based upon the error incurred in the acceleration field on the chosen Brillouin sphere, and (3) The gravitational potential and acceleration field are calculated using the determined radial location of the Brillouin sphere and the truncation degree.

An ideal Brillouin sphere radius and truncation degree are able to be determined as a function of a given orbit where the error in the acceleration field is locally minimized. The dual-density model for a contact binary is found to more accurately describe the dynamical environment around Asteroid 25143 Itokawa compared to the single density model.

ACKNOWLEDGEMENTS

I would first like to thank my advisor, Dr. Hitt, for always being excited and willing to help me with my work. Your enthusiasm inspired me to work harder. I would also like to thank my friends and colleagues, Jason Pearl and David Hinckley. Without both of your help and support, myself and this work would not have progressed to where it is at today. A big thank you as well to the Vermont Space Grant Consortium for funding my research over the past two under NASA Cooperative Agreement #NNX10AK674, with additional computing support from the Vermont Advanced Computing Center (NASA Cooperative Agreement #NNX06AC88G).

TABLE OF CONTENTS

List of Figures

CHAPTER 1

INTRODUCTION

Unmanned missions to small celestial objects, including near-Earth asteroids and comets, represent a significant component of the future of space exploration. These objects can be highly irregular in shape and have non-homogeneous density distributions causing their gravitational fields to be highly complex. Due to the close proximity of missions to these objects, precise trajectory planning is needed and thus an accurate gravity model is essential for mission success.

This thesis will address the challenges involved in modeling the gravitational field of small celestial objects by implementing a spherical harmonic potential model. A mascon distribution model is used as the baseline and input for the spherical harmonic series expansion. Details on the mascon distribution models used are available in the appendix (Appendix A) and supplemental papers referenced.

CONTACT BINARIES

Earth's neighborhood is littered with the remnants of the early Solar System. These objects are called "Near-Earth Objects" (NEOs) and are comprised of both asteroids and comets. Due to their small scale and high quantity, the frequency of collisions between NEOs are

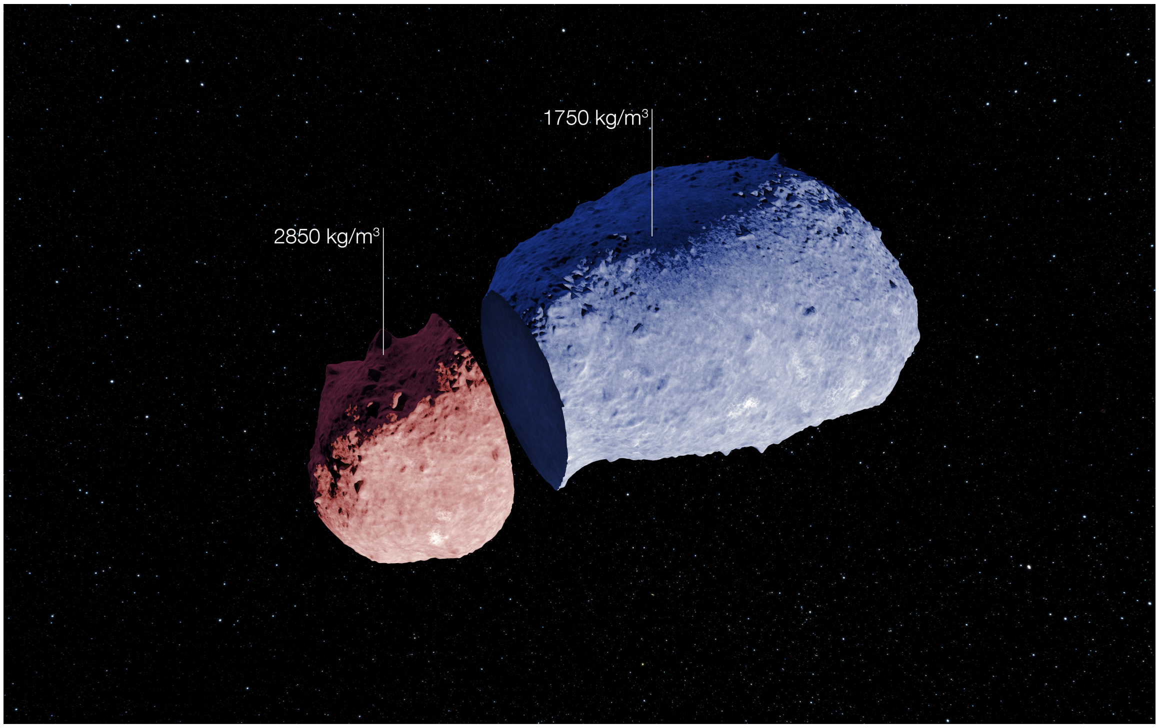

Figure 1.1: Diagram of asteroid 25143 Itokawa highlighting its two, homogeneous density regions. Credit: ESO [1].

high and cause them to constantly change in size and composition. When two objects aggregate into one, they are referred to as “contact binaries”. Contact binaries are assumed to contain two densities (one from each of the two bodies that collided).

Figure 1.1 highlights the possible differing density regions of asteroid 25143 Itokawa. The “head” of Itokawa (red) has a slight higher density than that of the “body” (blue).

Ongoing and Future Missions

Over the last few decades, there have been a wide range of missions to small celestial bodies such as comet 67P/Churyumov-Gerasimenko (67P/C-G), asteroid 101955 Bennu, and asteroid 25143 Itokawa. The first asteroid flyby was conducted by the *Galileo* spacecraft in 1991 [2]. Since then, dozens of comets and asteroids have been encountered and the

Table 1.1: Examples of missions to comets and asteroids.

Mission Name	**Space Agency**	**Launch Date**	**Target**	**Mission**
Galileo	NASA	October 1989	951 Gaspra	Jupiter Orbiter [3]
NEAR Shoemaker	NASA	February 1996	Eros	Orbiter [4]
Stardust	NASA	February 1999	81P/Wild & 9P/Tempel	Flyby & Sample Return [5]
Hayabusa	JAXA	May 2003	25143 Itokawa	Sample Return [6]
Rosetta	ESA	March 2004	67P/C-G	Orbiter/Lander [7]
Deep Impact	NASA	January 2005	9P/Tempel & 103P/Hartley	Flyby & Impactor [8]
Dawn	NASA	September 2007	Vesta & Ceres	Orbiter [9]
Hayabusa 2	JAXA	December 2014	162173 Ryugu	Sample Return [10]
OSIRIS-REx	NASA	September 2016	101955 Bennu	Sample Return [11]

intrigue of their origin and use has risen.

Table 1.1 lists various examples of previous missions to comets and asteroids and the objective of each mission. By returning samples and orbiting small bodies, our understanding of space flight and the origins of our Solar System have greatly increased.

There are multiple missions planned and proposed for the next decade including: NASA's Asteroid Redirect Mission (ARM), NEOCam, and Lucy. *Galileo* gave a good example of the necessity of understanding the dynamic environment around small bodies because although the mission end game may not be an asteroid or comet, in order to reach any part of the Solar System, asteroids/comets will be encountered.

Gravitational Potential

The gravitational potential induced on one spherical body from another can be calculated continuously as,

$$\Phi(r) = -\frac{Gm_1m_2}{\mathbf{r}} \tag{1.1}$$

where G is the gravitational constant ($6.6741\times10^{-11}\ m^3kg^{-1}s^{-2}$), m_1 and m_2 are the respective masses of the two bodies, and **r** is the position vector from one body to the other at any given instant. Typically the mass of the second body is considered negligible (as in the case of an orbiting spacecraft) and equation 1.1 can be reduced to,

$$\Phi(r) = -\frac{Gm_1}{\mathbf{r}} \tag{1.2}$$

For the case of asymmetric, non-spherical bodies, the gravitational potential must be computed by either appending perturbation forces to the point mass potential (Eq. 1.1) or using a finite element approach,

$$\Phi(\mathbf{r}) = -G \sum_{i=0}^{N} \frac{dm_i}{|\mathbf{r} - \mathbf{r_i}|} \tag{1.3}$$

where dm_i is the mass of the ith grid volume located within the body at position $\mathbf{r_i}$ (Figure 1.2). The denominator of equation 1.3 can be expanded via the law of cosines or using Legendre polynomials which will be discussed in Chapter 2.

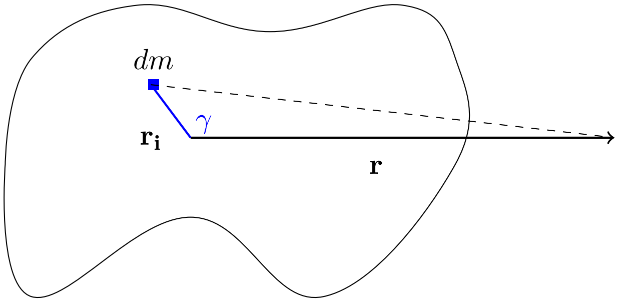

Figure 1.2: Diagram showing the gravitational potential an orbiting spacecraft experiences from a differential mass element, dm.

The potential expressions shown must satisfy either Laplace's or Poisson's equation.

Poisson's and Laplace's Equations

Poisson's equation describes the potential field induced by a given charge or density distribution,

$$\nabla^2\Phi = -4\pi G\rho \tag{1.4}$$

where G is the gravitational constant and ρ is the density distribution of the given body.

If the density distribution is zero, equation 1.4 can be reduced to Laplace's equation,

$$\nabla^2\Phi = 0 \tag{1.5}$$

The solution to Laplace's equation is a set of harmonic functions.

Available Gravity Field Models

The gravitational potential field of an asymmetric body is derived from a shape model of the body and can either be calculated discretely from each component of that shape model or it can be expanded as an infinite, convergent series. Both approaches hold merit, but are not without flaws. Prior works have examined various modeling techniques including: approximating the shape as a dumbbell (two mascons tangent to one another) [12], a homogeneous ellipsoid [13], the mascon model (filling the body with multiple small point masses) [14], and the polyhedron model [15, 16]. Due to the idealized nature of the first two methods, they can be applied to many bodies, but have the downside of oversimplifying the shape. The last two methods have the ability to model most body shapes with a high degree of accuracy, but this specification requires an in-depth knowledge of the characteristics of the body which is not always readily available.

Werner [17] was the first person to analytically calculate the gravity and acceleration fields of asteroids and comets by modeling the body as a constant-density polyhedron. In order to obtain a higher degree of accuracy of the shape of the body, Chanut et al. [18] presented two types of mass concentration (mascon) models: (1) A triangular face on the surface is extended to the center of the body to form a tetrahedron, and (2) That tetrahedron is split into three parts. This allowed for the volume of a given body to be modeled from surface elements which leads to variable density representation within a body. The mascon model decomposes the body into a collection of point masses and obtains the total potential field by the principle of superposition. The attractiveness of this model lies in its robustness, computational simplicity, and ability to be parallelized for speed. This approach has been previously used to calculate the potential fields for asteroids 4769 Castalia [16] and 101955 Bennu [19], and comet 67P/Churyumov-Gerasimenko (67P/C-G) [20].

Pearl & Hitt [14] proposed a method for distributing mascons based on finite volume meshes and examined the effects of mesh topology on the accuracy of the resultant mascon distributions. The mascon model was found to be less accurate than the polyhedron model at the surface of a body, but the accuracy is quickly skewed towards the mason model as the distance from the surface increases. Also, the finite volume mesh distributes mascons non-uniformly, allowing the volume of each mascon to vary, which speeds up the mesh generation process.

Alternatively, the potential for an asymmetric body can, in principle, be represented as a spherical potential augmented by the addition of a (finite) number of tesseral harmonics. For highly asymmetric bodies the number of tesseral harmonics required and the complexity of the model is significantly increased. The spherical harmonic-based approach has been previously used to calculate the potential and acceleration fields for asteroids 4769 Castalia and 101955 Bennu [19]. The method has been shown to model a body's gravity field with high accuracy, but when computing close proximity orbital trajectories, there is significant error introduced into the acceleration field which is propagated through each time step of the simulation [19, 21]. Takahashi & Scheeres [19] tried to mitigate the errors close to the surface of a body by using spheres ("Brillouin spheres") tangent to the body's surface and calculating series coefficients interior and exterior to the spheres. By using a polyhedral base model for the spherical harmonic expansion of the gravity field, errors seen in using the exterior gravity field were decreased with the use of interior gravity fields/tangent Brillouin spheres. This method is shown to be useful for landing trajectories, but errors on the order of 5% - 10% are still seen in the acceleration field on the surface of asteroids 101955 Bennu and 4769 Castalia for degree n ≥ 5 and a total surface mapping using this method would require a significant amount of time to simulate. Despite the higher accuracy seen in this model compared to others, it's utility lies in analyzing gravity field anomalies after the fact and not in-situ, on the fly calculations.

CHAPTER 2

SPHERICAL HARMONICS

Spherical harmonic functions are the solution to Laplace's equation on a spherical boundary and are denoted as $Y_n^m(\theta, \phi)$ where θ is the polar angle that ranges from $[0, \pi]$ and ϕ is the azimuthal angle that ranges from $[0, 2\pi]$. Spherical harmonic functions are written in terms of associated Legendre polynomials and can be normalized depending upon the application. The associated Legendre polynomials have the form, $P_n^m(x)$ where n is the degree of the polynomial and m is the order (Figure 2.1). For the special case of $m = 0$, the associated Legendre polynomials are referred to as Legendre polynomials, $P_n(x)$ (Figure 2.2).

FUNCTION CHARACTERISTICS

Spherical Harmonics define an orthonormal basis on a sphere and are defined as,

$$Y_n^m(\theta, \phi) = K_n^m e^{im\phi} P_n^m(cos\theta) \tag{2.1}$$

where n ϵ [0,N], m ϵ [-n,n], and K_n^m are the normalization constants.

In geodesy and spectral analysis applications, it is typical for the associated Legendre

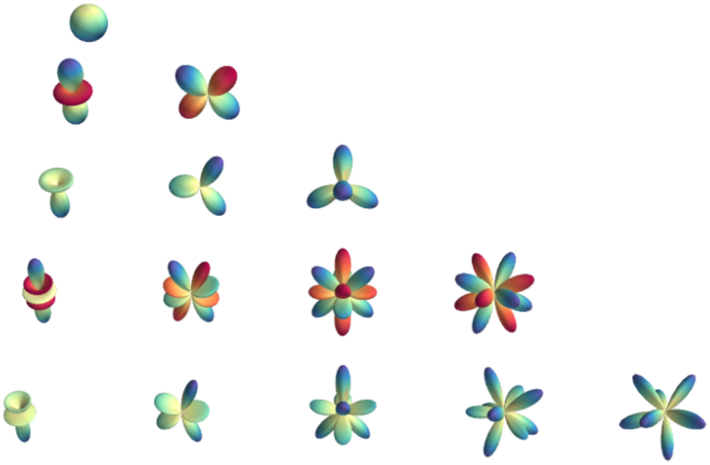

Figure 2.1: Visualization of real valued spherical harmonic modes ranging from n = m = [0,4].

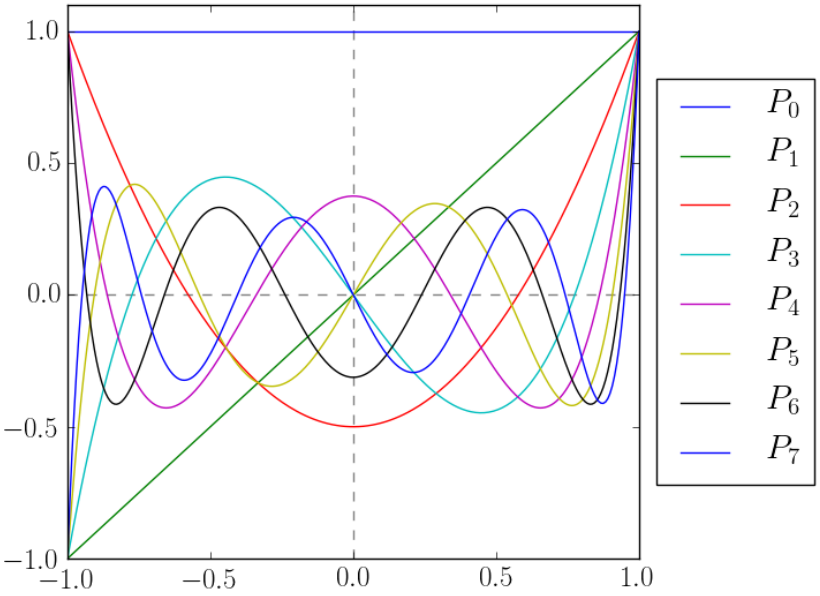

Figure 2.2: Visual of the Legendre polynomials for degrees n = 0,...,7.

polynomials and thus, the spherical harmonic functions, to be normalized by 4π such that,

$$K_n^m = \sqrt{(2n+1)\frac{(n-m)!}{(n+m)!}}$$

and,

$$\iint_\Omega Y_{nm}(\theta,\phi)Y^*_{n'm'}(\theta,\phi)d\Omega = 4\pi\delta_{nn'}\delta_{mm'}$$

Only the real components of the spherical harmonic functions are considered in geodesy and spectral analysis applications (the imaginary components of the functions are typically only used in Quantum Mechanical calculations). Therefore, the addition of a $(-1)^m$ term (referred to as the "Condon-Shortley Phase") in the spherical harmonic definition is neglected.

By only considering the real components of the spherical harmonic functions, the series undergoes an initial "triangular truncation", as seen in Figure 2.1. Further truncation of the series is required for practical applications of the infinite series. This truncation degree, N, will be determined in a case-by-case manner.

GRAVITATIONAL POTENTIAL

Referring back to equation 1.3, the denominator of this equation can be rewritten using the law of cosines as,

$$\begin{aligned}|\mathbf{r}-\mathbf{r_i}| &= \sqrt{r^2 - 2\mathbf{r}\cdot\mathbf{r_i} + r_i^2}\\ &= \frac{1}{r}\sqrt{1 - 2\frac{r_i}{r}\cos\gamma + \left(\frac{r_i}{r}\right)^2}\end{aligned}$$

This is now the generating function for Legendre polynomials and can be rewritten again as,

$$\frac{1}{r}\sqrt{1-2\frac{r_i}{r}\cos\gamma+\left(\frac{r_i}{r}\right)^2}=\frac{1}{r}\sum_{n=0}^{\infty}\left(\frac{r_i}{r}\right)^n P_n(\cos\gamma) \tag{2.2}$$

and thus the gravitational potential of an axisymmetric body can be written as,

$$\Phi(\mathbf{r})=-\frac{Gm}{r}\sum_{n=0}^{\infty}\left(\frac{r_i}{r}\right)^n P_n(\cos\gamma) \tag{2.3}$$

which reduces to Eq. 1.2 when $n=0$.

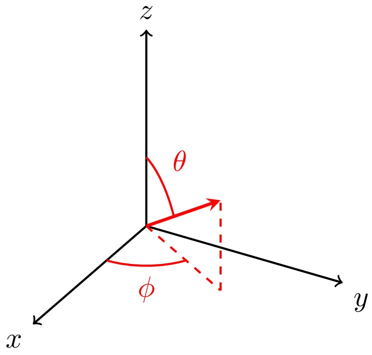

In order to obtain the general form of the gravitational potential equation written in spherical harmonics for asymmetric bodies, one of two methods can be used: MacCullagh's method [22] or spherical trigonometry [23]. The spherical trigonometry approach is more applicable to this thesis so that derivation will be highlighted here.

From Eq. 2.3, $\cos(\gamma)$ can be expanded as,

$$\cos(\gamma)=\mathbf{r}\cdot\mathbf{r_i}=\sin(\theta)sin(\theta')\cos(\phi-\phi')+\cos(\theta)\cos(\theta')$$

where $\mathbf{r}=\sin(\theta)\cos(\phi)\hat{\imath}+\sin(\phi)\sin(\theta)\hat{\jmath}+\cos(\theta)\hat{k}$ and similarly for $\mathbf{r_i}$. Using the addition theorem for Legendre polynomials, $P_n(\cos\gamma)$ can be written as,

$$P_n(\cos\gamma) = P_n(\cos\theta)P_n(\cos\theta') + 2\sum_{m=1}^{n}\frac{(n-m)!}{(n+m)!}[A_{n,m}A'_{n,m} + B_{n,m}B'_{n,m}] \tag{2.4}$$

where

$$\begin{aligned} A_{n,m} &= P_n^m(\cos\theta)\cos(m\phi) \\ B_{n,m} &= P_n^m(\cos\theta)\sin(m\phi) \\ A'_{n,m} &= P_n^m(\cos\theta')\cos(m\phi') \coloneqq C'_{n,m} \\ B'_{n,m} &= P_n^m(\cos\theta')\sin(m\phi') \coloneqq S'_{n,m} \end{aligned}$$

and $C'_{n,m}$ and $S'_{n,m}$ are the series coefficients normalized by the reference radius, r_i^n, and body mass.

Plugging Eq. 2.4 into Eq. 2.3 and simplifying gives the gravitational potential field for axisymmetric and asymmetric modes,

$$\begin{aligned} \Phi(\mathbf{r}) = -\frac{Gm}{r}\Big[\sum_{n=0}^{\infty}\left(\frac{r_i}{r}\right)^n C_n^0 P_n(\cos\theta) + \sum_{n=1}^{\infty}\sum_{m=1}^{\infty}\left(\frac{r_i}{r}\right)^n \\ P_n^m(\cos\theta)[C'_{n,m}\cos(m\phi) + S'_{n,m}\sin(m\phi)]\Big] \end{aligned} \tag{2.5}$$

C_n^0 corresponds to the coefficients for the axisymmetric modes (zonal harmonics) and are typically written as J_n, where $J_n = -\left(\frac{r_i}{r}\right)^n C_n^0$.

CHAPTER 3

COMPUTATIONAL METHODS

A given body is decomposed into multiple, discrete, spherical mass concentrations ("mascons") (Appendix A). The gravitational potential of the body is then discretely calculated from each finite element (Eq. 1.3) and projected onto a circumscribing spherical boundary called a "Brillouin sphere". The projected potential on the boundary can then be expanded as an infinite series of spherical harmonic functions via,

$$\Phi(\mathbf{r}) = -\frac{\mu}{R_S}\Big[\sum_{n=0}^{N}\sum_{m=0}^{n}\left(\frac{R_S}{r}\right)^{(n+1)} P_n^m(\cos\theta)[C_n^m\cos(m\phi) + S_n^m\sin(m\phi)]\Big] \tag{3.1}$$

where R_S is the radius of the Brillouin sphere. The Brillouin sphere boundary and differing model regions can be seen in Figure 3.1. If the body contains regions of variable density, the corresponding mascons will be tagged with the appropriate density when calculating the gravitational potential induced by that mascon. For the case of contact binaries, the body can be split into two, homogeneous density subsections and their potential fields can be expanded individually. If the body is assumed to be of homogeneous density, each mascon is tagged with the bulk density of the body and the potential field is calculated in its entirety.

Once the coefficients of the spherical harmonic series expansion are calculated, the potential fields can be numerically integrated to obtain orbital trajectories about the body. Due to the linearity of spherical harmonic functions, if the body has been decomposed into variable density subsections, the acceleration fields can be summed to obtain the full acceleration field of the body and therefore a complete trajectory.

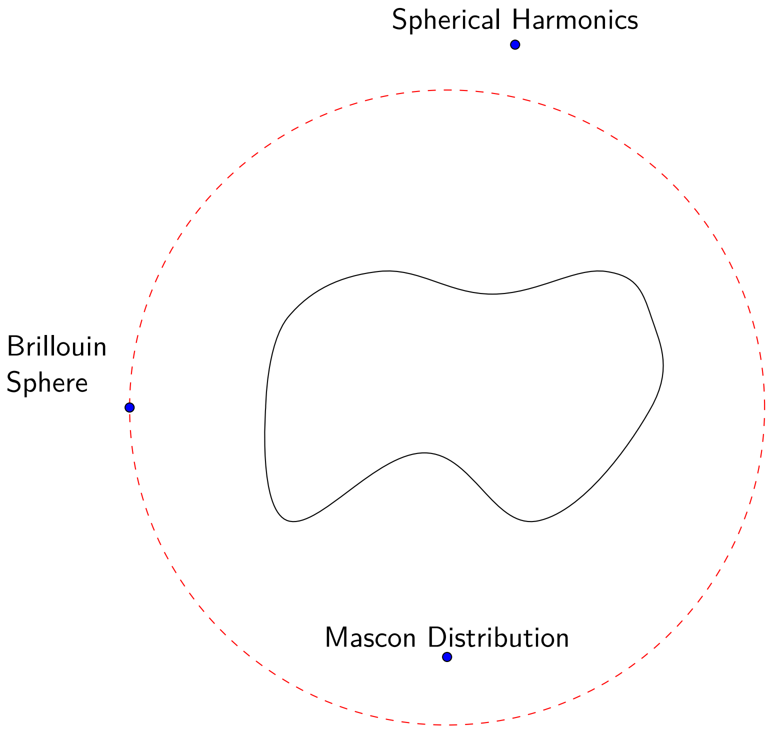

Figure 3.1: Diagram depicting the potential matching on the Brillouin sphere.

Coefficient Determination

The gravitational potential field of any body can be expressed in terms of a spherical harmonic series expansion as long as the boundary of this field is a spherical surface. The Brillouin sphere acts as this boundary.

The Brillouin sphere map is fully defined by its resolution, spacing, and radius. The resolution of the Brillouin sphere is determined by the resolution of the base mascon distribution and must be spaced in such a way as to allow for the inversion technique used to calculate the coefficients of the series. A Gauss-Legendre Quadrature inversion is used here and requires a $[\theta, \phi] \epsilon$ [N+1,2N+1] spaced grid, where N is the maximum degree of the spherical harmonic series.

Once the potential field is correctly projected onto the Brillouin sphere, the field can undergo modal decomposition (via Gauss-Legendre Quadrature (GLQ)) to determine the coefficients, C_n^m and S_n^m, that uniquely define the system. A benefit of using this quadrature method is that aliasing of the data is not a factor [24].

GLQ assumes that an integral of the form,

$$\int_a^b f(x)dx$$

can be approximated as,

$$\sum_{i=1}^{n} w_i f(x_i)$$

where w_i and x_i are the weighting coefficients and the nodes of the series respectively. The integral must be normalized such that $a = -1$ and $b = 1$. This definition can easily be extended to multidimensional applications,

$$\int_{-1}^{1}\int_{-1}^{1} f(x,y)dxdy \approx \sum_{i=1}^{n}\sum_{j=1}^{m} w_{i,j} f(x_i, y_j) \tag{3.2}$$

For the case of spherical harmonics,

$$f(\theta,\phi) = \sum_{n=0}^{\infty}\sum_{m=0}^{n} A_n^m Y_n^m(\theta,\phi) \tag{3.3}$$

where A_n^m are the coefficients of the series (i.e. C_n^m and S_n^m) left to be determined.

Up to N coefficients are able to be calculated using this method, but in practice, this many are not needed. The exact number of coefficients needed will be discussed in Chapter 4.

The open source python toolbox, *SHTOOLS* [25], is used to implement the GLQ inversion. The coefficients are 4π-normalized and the Condon-Shortley phase is neglected.

ACCELERATION

Once the gravitational potential field is established as a finite series of spherical harmonics (i.e. the coefficients of the series, C_n^m and S_n^m, are determined), the acceleration of an orbiting body can be expressed in Cartesian coordinates as,

$$\begin{aligned}
a \equiv &- \nabla\Phi(x,y,z) = -\frac{\mu}{R_S}\sum_{n=0}^{N}\sum_{m=0}^{n} R_S^{n+1}(x^2+y^2+z^2)^{\frac{-(n+2)}{2}} \\
&\begin{bmatrix} \frac{xz}{x^2+y^2} \\ \frac{yz}{x^2+y^2} \\ \sqrt{x^2+y^2+z^2} \end{bmatrix} \Bigg((n-m+1)P_{n+1}^m\left(\frac{z}{\sqrt{x^2+y^2+z^2}}\right) \\
&\begin{bmatrix} \cos(m\zeta)+\sin(m\zeta) \\ \cos(m\zeta)+\sin(m\zeta) \\ \sin(m\zeta)-\cos(m\zeta) \end{bmatrix} \begin{bmatrix} C_n^m \\ S_n^m \end{bmatrix} + \sqrt{x^2+y^2+z^2}P_n^m\left(\frac{z}{\sqrt{x^2+y^2+z^2}}\right) \\
&\begin{bmatrix} -(C_n^m x(n+1)+S_n^m my) & (C_n^m my - S_n^m x(n+1)) \\ (C_n^m y(n+1)+S_n^m mx) & -(C_n^m mx + S_n^m y(n+1)) \\ 0 & 0 \end{bmatrix} \begin{bmatrix} \cos(m\zeta) \\ \sin(m\zeta) \end{bmatrix}\Bigg), \qquad (3.4)
\end{aligned}$$

$$\zeta \equiv \arctan(\tfrac{y}{x})$$

where μ is the gravitational parameter of the body and R_S is the radius of the Brillouin sphere. The acceleration field is converted from Spherical to Cartesian coordinates for computational implementation.

In order to account for a body's rotation, a rotation tensor about the z-axis can be used. For sake of comparison between models, rotation is ignored in the following chapters.

CHAPTER 4

METHOD CHARACTERIZATION

Two bodies of interest were chosen to characterize the utility and scope of this spherical harmonic model: Earth and Asteroid 101955 Bennu. Earth was chosen because it's zonal harmonics are well defined and Bennu was chosen because of its smaller size and more dynamical environment, as well as its current interest in the science community due to the OSIRIS-REx launch last year.

EARTH

Three trajectories are chosen to analyze the behavior of the model in different environments around Earth: a low Earth orbit (LEO), medium Earth orbit (MEO), and an orbit inclined to Earth's equatorial plane. Each of these orbits are used to quantify and characterize the error in the potential and acceleration fields derived from this spherical harmonic model in comparison to the experimentally derived zonal harmonics for Earth. The orbits are also used as a way to define an ideal location/radius for the Brillouin sphere.

LEO

A circular LEO orbit of altitude $r = 200$ km is simulated (Figure 4.1).

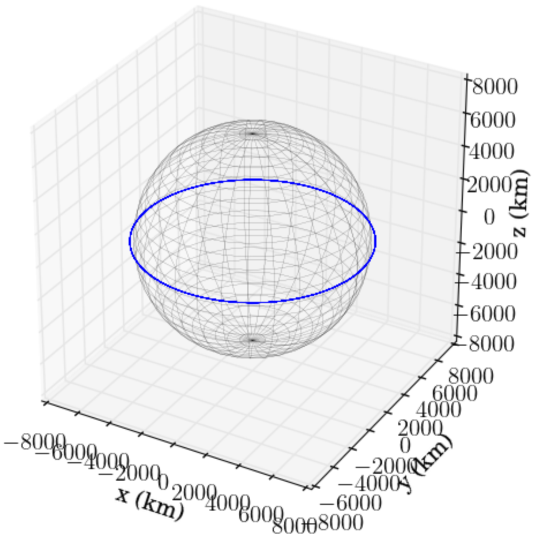

Figure 4.1: LEO orbit with altitude of 200 km.

Brillouin Sphere Radius

The radius of the Brillouin sphere is typically desired to be as close to the surface of a given body as possible. This allows for close proximity trajectory calculations to be done using the spherical harmonic model, but this radial location may not be ideal when it comes to minimizing the error incurred in gravity and acceleration field calculations.

The radius of the Brillouin sphere, R_S, is allowed to vary between 5% and 95% of the orbital altitude of the trajectory being simulated with the constraint that periapsis cannot cross the spherical boundary. At each location, the error in the potential field and acceleration field is analyzed as a function of truncation degree of the spherical harmonic series. Figure 4.2 shows the mean percent difference between the harmonic derived and the theoretical potential field of Earth on each Brillouin sphere radius. The mean percent difference error (MPE) is calculated from two series truncation degrees: N = 8 and 15.

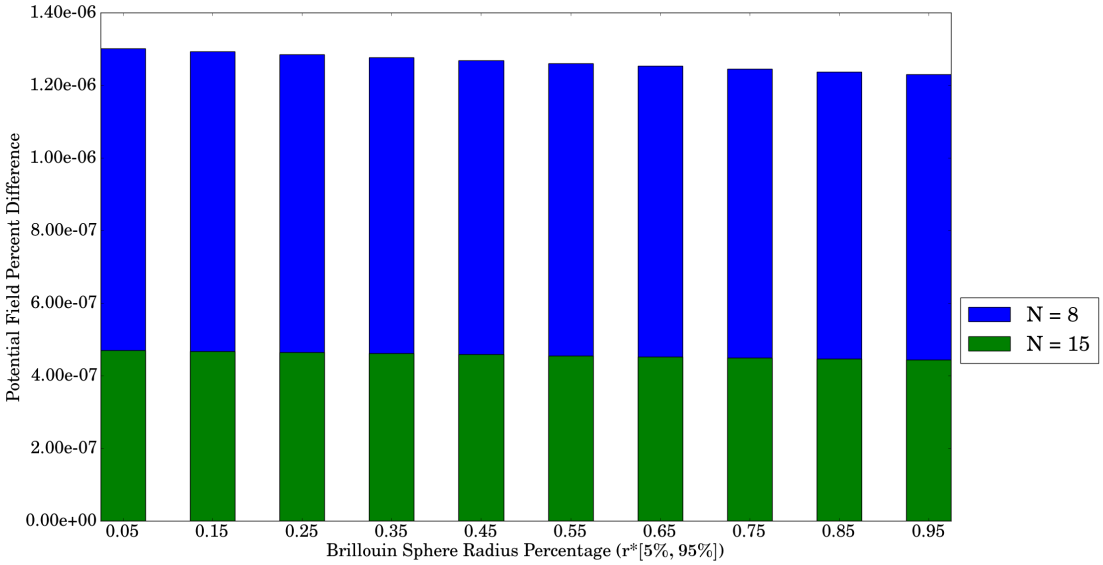

Figure 4.2: Mean percent difference in the gravitational potential derived from spherical harmonic model and degrees N = 8 and 15 on each Brillouin sphere.

These truncation degrees were chosen based on the limits of the known zonal harmonics (up to J_7) and the limits of the numerical inversion algorithm (up to N = 15 based on the normalization of the series). The error in the derived potential field is shown to decrease as the degree of the series is increased as well as the radius of the Brillouin sphere.

Figure 4.3 shows the error in the acceleration field on each Brillouin sphere radius using the maximum truncation degree of N = 15. At $R10 = R_{10}/r = 95\%$, the error in the acceleration field is at its lowest with a value of $5.88 \times 10^{-4}\%$. The difference between the acceleration field errors can be better seen in Figure 4.4 which shows the increasing trend in the -$\log_{10}$(MPE) which correlates to a decreasing trend in error on spheres R_8, R_9, and R_{10}. The error in the acceleration field mirrors the results of the errors in the potential field leading to the conclusion that the largest Brillouin sphere (the sphere closest to the simulated trajectory), $R_{10}/r = 95\%$, will give the most accurate results.

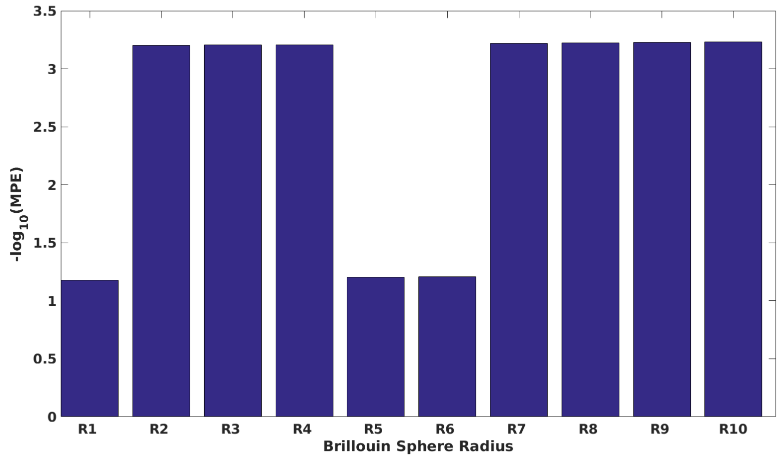

Figure 4.3: The -log$_{10}$ of the mean percent difference in the acceleration field derived from the theoretical zonal harmonics of Earth and the spherical harmonic model on each Brillouin sphere for the maximum truncation degree (N = 15).

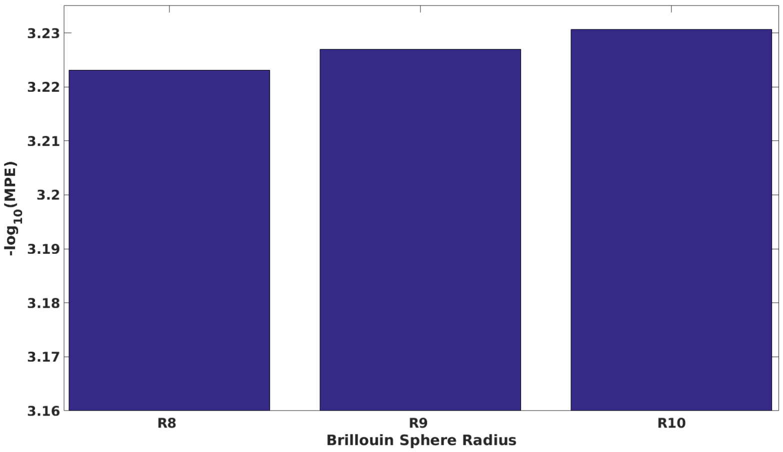

Figure 4.4: Zoomed in view of error in the acceleration field on the three largest Brillouin sphere radii analyzed: R_8, R_9, and R_{10}.

Table 4.1: Comparison of the theoretical zonal harmonics and derived coefficients for a LEO orbit on a Brillouin sphere of radius $R_s/r = 95\%$.

	$\mathbf{J}_n$	$\mathbf{J}_n^{10}$	**Percent Difference**
J_2	$1.082\,63 \times 10^{-3}$	$1.082\,92 \times 10^{-3}$	2.6787×10^{-2}
J_3	$-2.532\,66 \times 10^{-6}$	$2.875\,67 \times 10^{-6}$	13.543
J_4	$-1.619\,63 \times 10^{-6}$	$-1.846\,03 \times 10^{-6}$	13.979
J_5	$-2.272\,98 \times 10^{-7}$	$3.130\,29 \times 10^{-7}$	37.717
J_6	$5.406\,76 \times 10^{-7}$	$4.498\,11 \times 10^{-7}$	16.806
J_7	$3.523\,64 \times 10^{-7}$	$-3.078\,61 \times 10^{-7}$	12.629

Series Coefficient Determination

The zonal harmonics, J_n, for Earth are compared to the derived coefficients for this orbit using $R_{10}/r = 95\%$ in Table 4.1. The theoretical zonal harmonics can be compared to the derived harmonic coefficients via, $J_n = -\left(\frac{R_S}{r}\right)^n C_n^0 := J_n^S$ where $J_n^S = J_n^{10}$ for the Brillouin sphere used. There is a good correlation between the experimental and theoretical zonal harmonics, but as the precision of the coefficients increases, the model has a harder time matching the "true" value.

Similar to Figure 4.3, Figure 4.5 shows the error in the acceleration field on each Brillouin sphere for this orbit, but now the relative errors in the truncation degree are also being compared. Degrees N = 3, 5, 7, 10, 12, and 15 are shown. Their resultant acceleration field errors on each sphere overlap almost completely. For the chosen Brillouin sphere, R_{10}/r, N = 5 gives the smallest error in the acceleration field with a value of $6.0718 \times 10^{-4}\%$.

Orbital Parameters

A useful comparative tool for the accuracy of the final trajectory output by the model is the time evolution of the orbital parameters. There are six Keplerian elements: semi-major axis (a), specific true anomaly (ν), argument of perigee (ω), right ascension of the ascending node (Ω), eccentricity (e), and inclination (i). The specific angular momentum

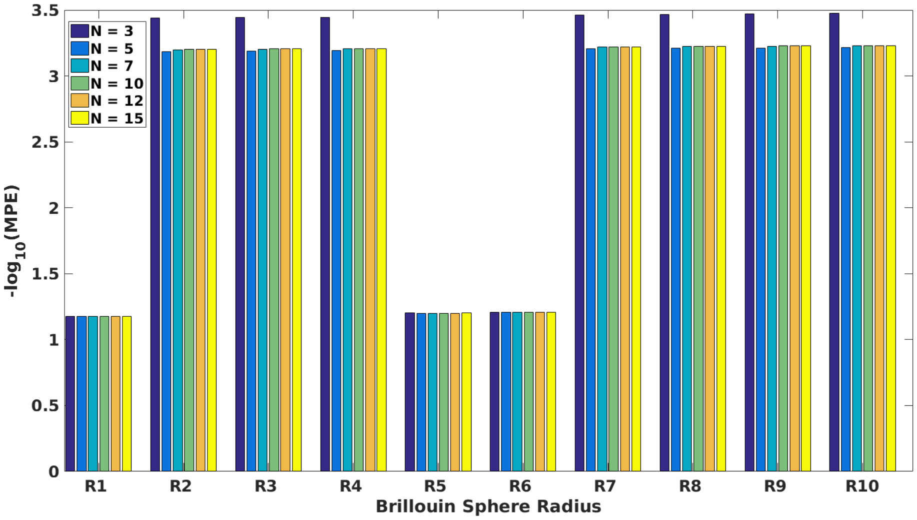

Figure 4.5: The -log$_{10}$ *of the mean percent difference in the acceleration field derived from the theoretical zonal harmonics of Earth and the spherical harmonic model on each Brillouin sphere for truncation degrees N = 3, 5, 7, 10, 12 and 15.*

(h) is another useful metric for analyzing an orbital trajectory. Only three are plotted in Figure 4.6 (h, e, and i) to reduce visual clutter. The relative differences between all of the parameters and the "true" parameter values are listed in Table 4.2.

The change in inclination shown in Figure 4.6 shows the largest variances between the output from each degree, N. N = 3 undershoots the "true" inclination and N = 5 overshoots it. After N = 8, the values converge upon each other which means a higher accuracy output based on increasing the truncation degree further is not possible. The specific angular momentum and eccentricity plots are much less sensitive to perturbations in the data set as there are no differences between the differing degree outputs.

Although N = 5 gave the highest precision acceleration field, it does not give the most accurate orbital parameters. N = 8 is chosen as the ideal truncation point of the series for this orbit. This truncation degree is expected based upon the defined zonal harmonics for Earth (up to $J_7 = -\left(\frac{R_S}{r}\right)^7 C_7^0$).

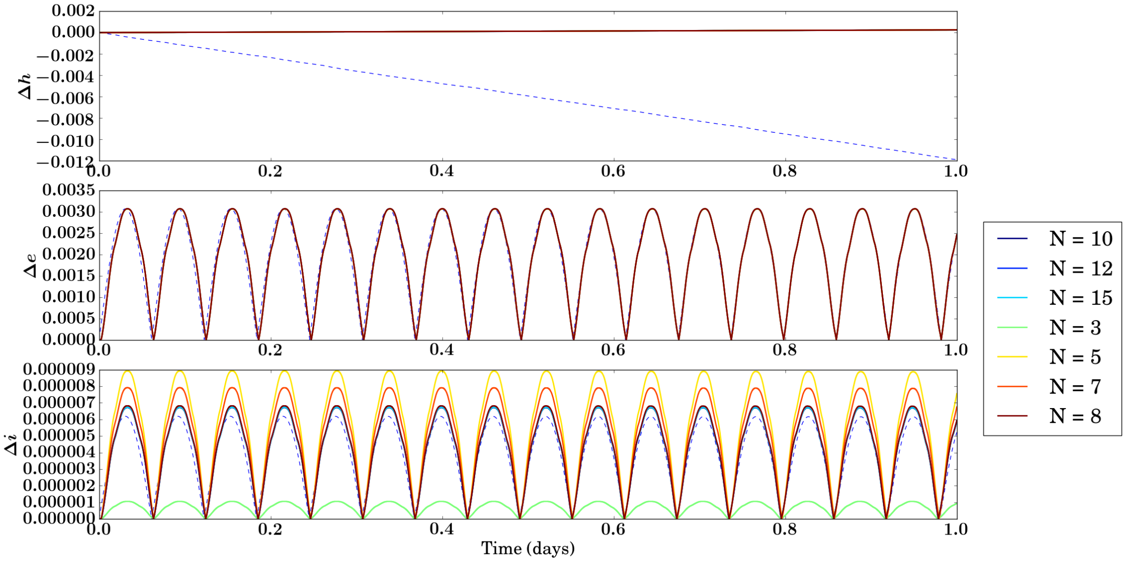

Figure 4.6: Comparison of the change in the time evolution of orbital parameters for a LEO orbit. The dashed line shows the "true" output and the colored lines are derived from various truncation degrees of the spherical harmonic series. A Brillouin sphere radius of $R_S/r = 95\%$ was used.

Table 4.2: Mean differences between the "true" and harmonic model derived evolution of orbital parameters for various truncation degrees, N.

Parameter	**N**						
	3	5	7	8	10	12	15
h	0.3952668	0.3952678	0.3952676	0.3952674	0.3952674	0.3952674	0.3952674
e	0.000115309	0.000115473	0.000115608	0.000115607	0.000115629	0.000115613	0.000115615
i	$3.241\,544 \times 10^{-6}$	$1.739\,987 \times 10^{-6}$	$1.124\,686 \times 10^{-6}$	$4.842\,694 \times 10^{-7}$	$4.275\,196 \times 10^{-7}$	$4.683\,980 \times 10^{-7}$	$4.367\,380 \times 10^{-7}$
ω	3.0277318	3.0926497	3.0831996	3.0581932	3.0536532	3.0580166	3.0538196
Ω	3.0812163	3.1010139	3.1004807	3.0946122	3.0932406	3.0945655	3.0932855

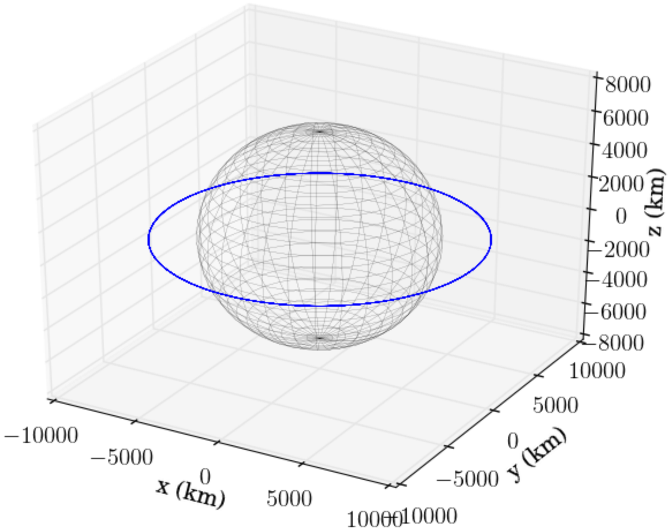

Figure 4.7: MEO orbit with altitude of 2000 km.

MEO

A circular MEO orbit of altitude $r = 2000$ km is simulated. The behavior of this orbit is analyzed in the same manner as the LEO orbit. The error in the gravitational potential and acceleration fields are analyzed as a function of the radius of the Brillouin sphere and truncation degree of the series. The time evolution of the orbital parameters is used as the final characterization of the accuracy of the model for this orbit.

Brillouin Sphere Radius

Figure 4.8 shows the mean percent difference between the harmonic derived and the theoretical potential field of Earth on each of the ten Brillouin sphere radii ($\frac{R_S}{r}\epsilon[5\%, 95\%]$). The same downward trend in error that was seen for the LEO orbit is seen here; as the Brillouin sphere radius is increased and a higher degree of the series is used, the error in

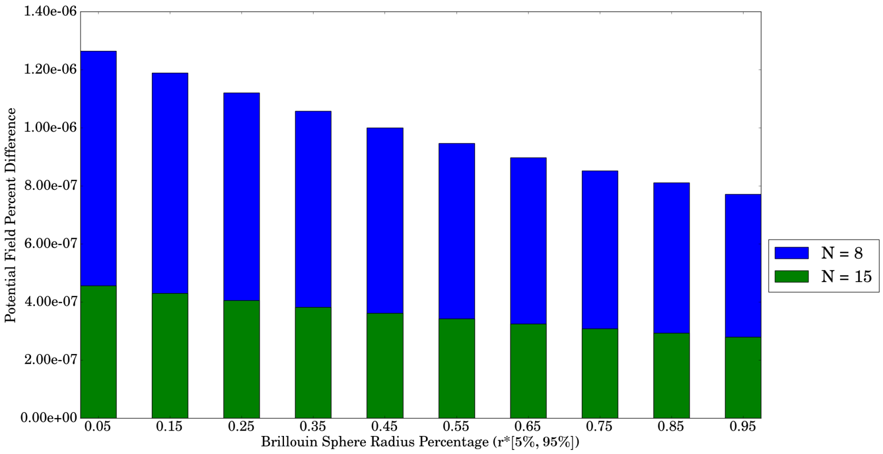

Figure 4.8: Mean percent difference in the gravitational potential derived from spherical harmonic model and degrees N = 8 and 15 on each Brillouin sphere.

the derived potential field decreases. There is a steeper downward slope seen here due to the larger orbital altitude and thus a larger range of R_S/r.

Figure 4.9 shows the error in the acceleration field on each Brillouin sphere radius using the maximum truncation degree of N = 15. The downward trend in error seen in the potential field is reversed for the acceleration field and the error at the smallest Brillouin sphere, $R1 = R_1/r = 5\%$, is actually less than the largest. R_1/r has a mean percent difference error of $1.0 \times 10^{-3}\%$ and at $R10 = R_{10}/r = 95\%$, the error in the acceleration field is $7.0 \times 10^{-3}\%$. Although there is a slight increase in the amount of error incurred in the acceleration calculations when using R_{10}/r, the lower error in the potential field at R_{10}/r warrants the use of that radius. However, errors in the coefficients and resulting orbital parameters for both radii will be considered in the following sections.

Series Coefficient Determination

The zonal harmonics, J_n, for Earth are compared to the derived coefficients for this orbit using R_1/r and R_{10}/r in Tables 4.3 and 4.4. There is a good correlation between the exper-

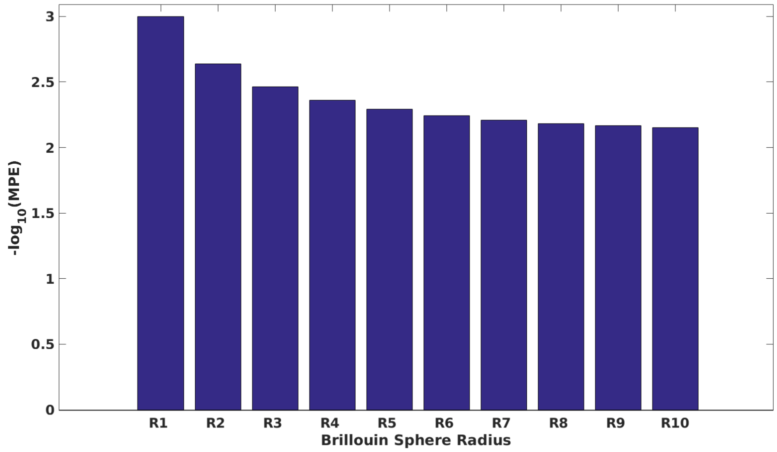

Figure 4.9: The -log$_{10}$ of the mean percent difference in the acceleration field derived from the theoretical zonal harmonics of Earth and the spherical harmonic model on each Brillouin sphere for the maximum truncation degree (N = 15).

Table 4.3: Comparison of the theoretical zonal harmonics and derived coefficients for a MEO orbit on a Brillouin sphere of radius $R_s/r = 5\%$.

	$\mathbf{J}_n$	$\mathbf{J}_n^5$	**Percent Difference**
J_2	1.08263×10^{-3}	1.08292×10^{-3}	2.6787×10^{-2}
J_3	-2.53266×10^{-6}	2.87101×10^{-6}	13.359
J_4	-1.61963×10^{-6}	-1.83983×10^{-6}	13.596
J_5	-2.27298×10^{-7}	3.09448×10^{-7}	36.142
J_6	5.40676×10^{-7}	4.54771×10^{-7}	15.888
J_7	3.52364×10^{-7}	-3.10826×10^{-7}	11.788

imental and theoretical zonal harmonics, but as the precision of the coefficients increases, the model has a harder time matching the “true” value. The coefficients derivations on both spheres have the hardest time matching J_5. J_2 is matched with the highest accuracy which proves well for the simulations seeing as that is the largest perturbation for Earth.

Figure 4.10 shows the error in the acceleration field across all Brillouin sphere radii, for various truncation degrees of the series (N = 3, 5, 7, 10, 12 and 15). The errors from each degree converge upon each other as the radius of the Brillouin sphere increases, so at R_{10}/r, there is no “optimal” choice for N when trying to minimize the error in the acceleration

Table 4.4: Comparison of the theoretical zonal harmonics and derived coefficients for a MEO orbit on a Brillouin sphere of radius $R_s/r = 95\%$.

	$\mathbf{J}_n$	$\mathbf{J}_n^{10}$	**Percent Difference**
J_2	$1.082\,63 \times 10^{-3}$	$1.082\,92 \times 10^{-3}$	2.6787×10^{-2}
J_3	$-2.532\,66 \times 10^{-6}$	$2.964\,22 \times 10^{-6}$	17.039
J_4	$-1.619\,63 \times 10^{-6}$	$-1.979\,81 \times 10^{-6}$	22.238
J_5	$-2.272\,98 \times 10^{-7}$	$4.014\,49 \times 10^{-7}$	76.618
J_6	$5.406\,76 \times 10^{-7}$	$3.089\,84 \times 10^{-7}$	42.852
J_7	$3.523\,64 \times 10^{-7}$	$-2.107\,64 \times 10^{-7}$	40.186

field. Looking at R_1/r though, N = 5 gives the smallest error at $9.957 \times 10^{-4}\%$.

Orbital Parameters

Similar to the LEO orbit, the change in inclination shown in Figures 4.11 and 4.12 show the largest deviations between the output from each degree, N. N = 3 undershoots the "true" inclination and N = 5 overshoots it just as they did in the LEO orbit. After N = 8, the values converge upon each other which means a higher accuracy output based on increasing the truncation degree further is not possible. The inclination derived from the spherical harmonic model using R_{10}/r matches the true inclination by ~ 2 times better on average than that of R_1/r. The specific angular momentum and eccentricity plots are much less sensitive to perturbations in the data set as there are no differences between the differing degree outputs.

The output eccentricity from R_{10}/r undershoots the true eccentricity by $\sim 10^{-4}$ on average whereas the spherical harmonic derived eccentricity using R_1/r matches the true eccentricity well for all truncation degrees.

A truncation degree of N = 8 is again chosen as the ideal point to terminate the series. Although the orbital parameter outputs from both Brillouin sphere radii are very similar, R_{10}/r gives a higher accuracy in the output inclination, as well as the derived potential field, so the largest radius will be designated as the ideal Brillouin sphere radius for this

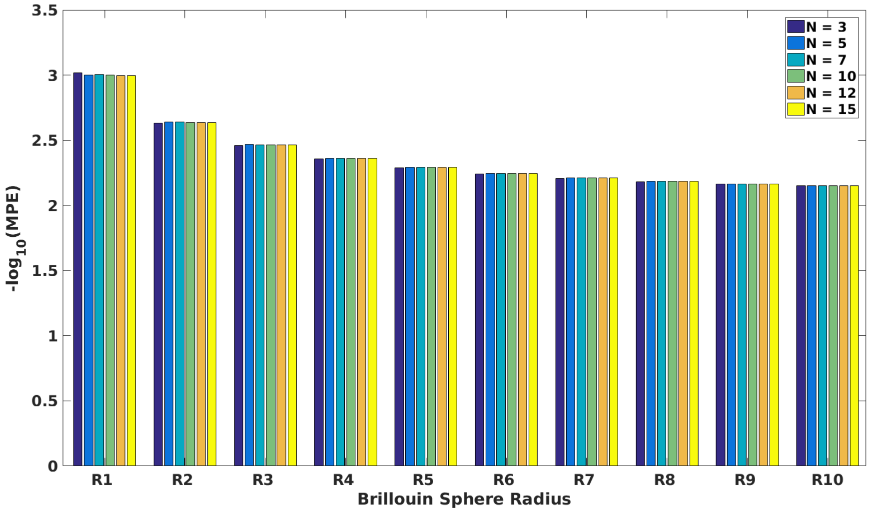

Figure 4.10: The -$\log_{10}$ of the mean percent difference in the acceleration field derived from the theoretical zonal harmonics of Earth and the spherical harmonic model on each Brillouin sphere for truncation degrees $N = 3$, 5, 7, 10, 12 and 15.

orbit.

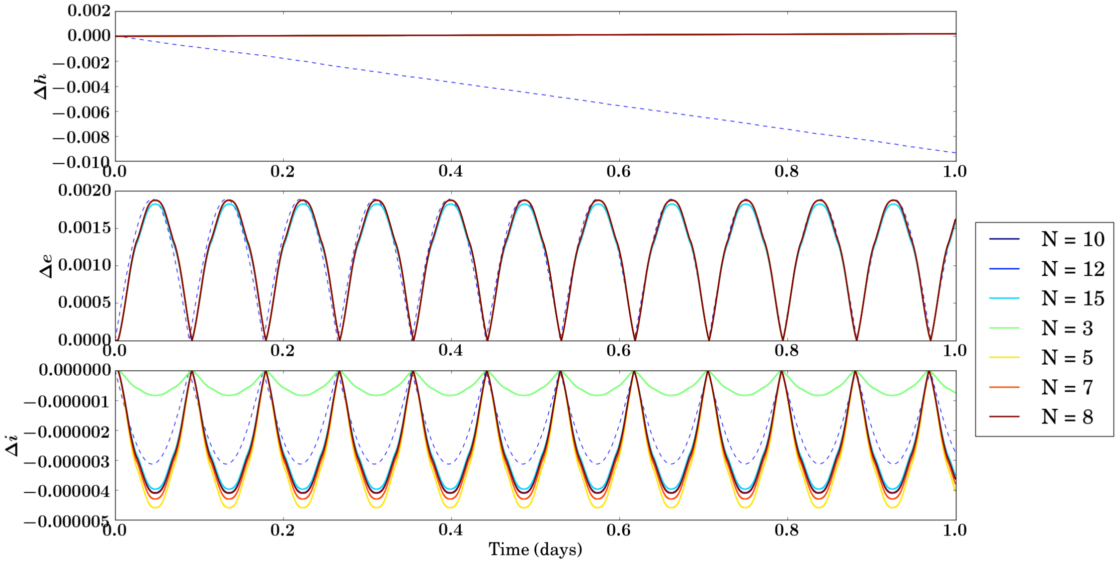

Figure 4.11: Comparison of the change in the time evolution of orbital parameters for a MEO orbit. The dashed line shows the "true" output and the colored lines are derived from various truncation degrees of the spherical harmonic series. A Brillouin sphere radius of $R_S/r = 5\%$ was used.

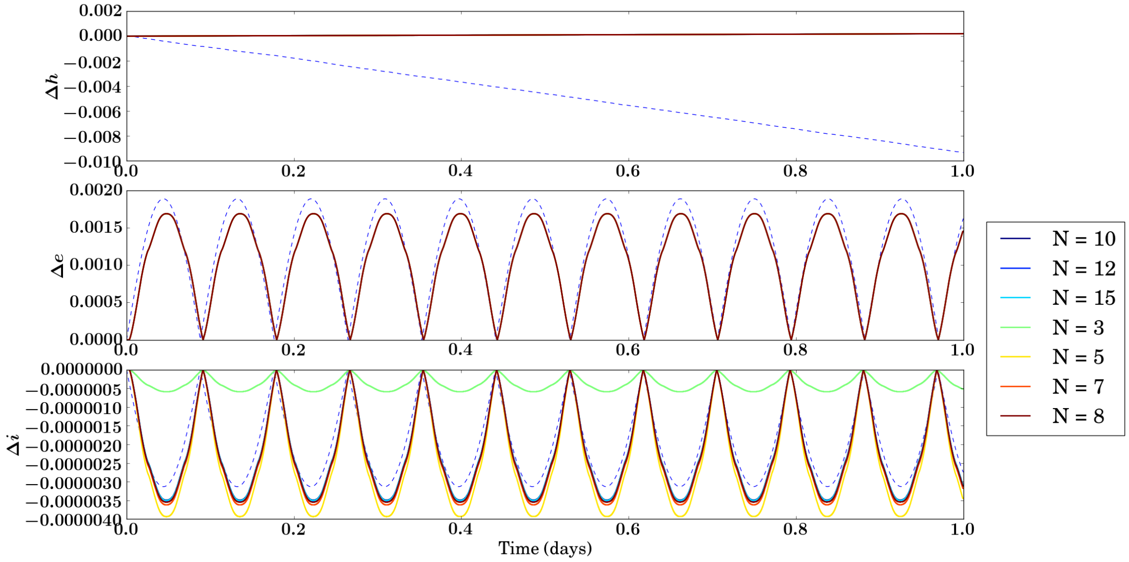

Figure 4.12: Comparison of the change in the time evolution of orbital parameters for a MEO orbit. The dashed line shows the "true" output and the colored lines are derived from various truncation degrees of the spherical harmonic series. A Brillouin sphere radius of $R_S/r = 95\%$ was used.

Inclined Orbit

A circular orbit inclined to Earth's equatorial plane by $i = 45°$ is simulated.

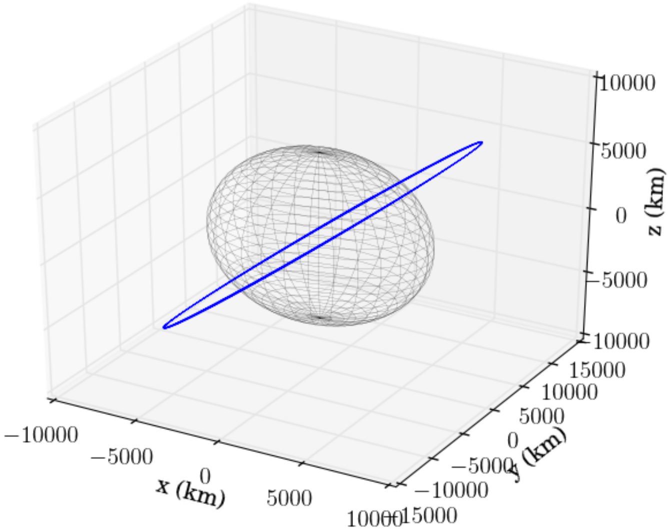

Figure 4.13: Orbit inclined at 45° to the equatorial plane with altitude of ∼2828 km.

Brillouin Sphere Radius

Figure 4.14 shows the mean percent difference between the harmonic model derived and the "true" potential field of Earth for degrees N = 8 and 15 of the harmonic series. Again the lowest error is seen in the largest Brillouin sphere for a higher truncation degree of the series (N = 15).

Figure 4.15 shows the error in the acceleration field on each of the ten Brillouin spheres for degree N = 15. As with the MEO orbit, the error incurred in the acceleration field calculations is less for the smaller Brillouin sphere, R_1/r, than the largest, R_{10}/r. R_1/r results in 0.0158 times less percent error in the acceleration field than R_{10}/r.

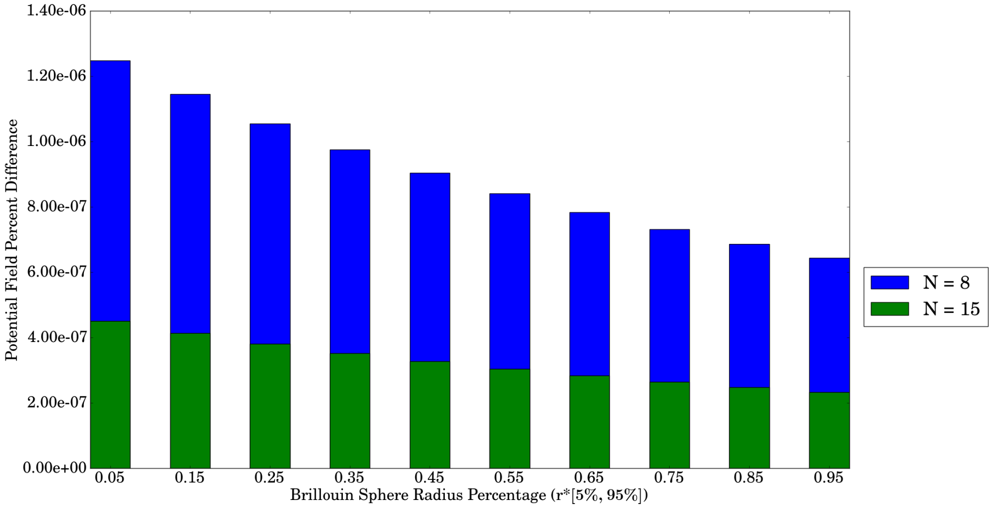

Figure 4.14: Mean percent difference in the gravitational potential field derived from the spherical harmonic model and degrees $N = 8$ and 15 on each Brillouin sphere.

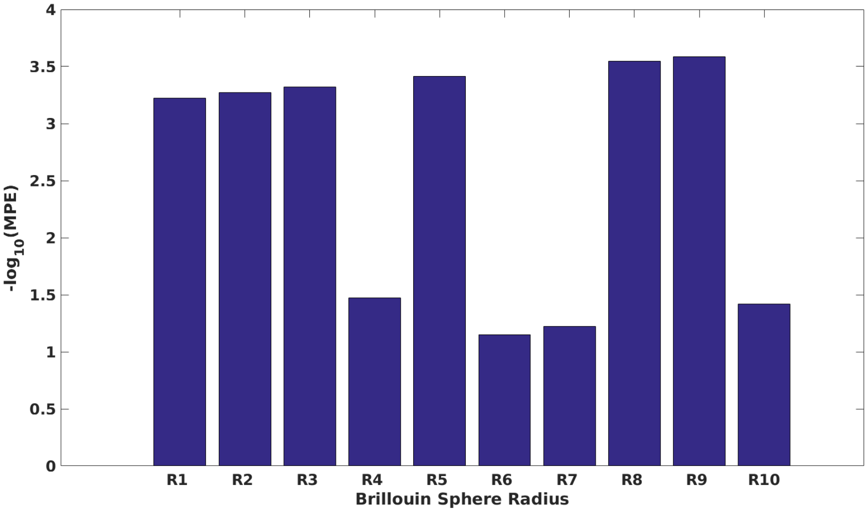

Figure 4.15: The -log_{10} of the mean percent difference in the acceleration field derived from the theoretical zonal harmonics of Earth and the spherical harmonic model on each Brillouin sphere for truncation degree $N = 15$.

Series Coefficient Determination

There again is a good correlation between the derived coefficients and the defined zonal harmonics on $R_{10}/r = 95\%$ where the most precise coefficient is J_2. Again the spherical

Table 4.5: Comparison of the theoretical zonal harmonics and derived coefficients for an inclined orbit on a Brillouin sphere of radius $R_s/r = 95\%$.

	$\mathbf{J}_n$	$\mathbf{J}_n^{10}$	**Percent Difference**
J_2	$1.082\,63 \times 10^{-3}$	$1.082\,92 \times 10^{-3}$	2.6787×10^{-2}
J_3	-$2.532\,66 \times 10^{-6}$	$3.004\,98 \times 10^{-6}$	18.649
J_4	$-1.619\,63 \times 10^{-6}$	$-2.051\,70 \times 10^{-6}$	26.677
J_5	$-2.272\,98 \times 10^{-7}$	$4.567\,70 \times 10^{-7}$	100.96
J_6	$5.406\,76 \times 10^{-7}$	$2.067\,139 \times 10^{-7}$	61.768
J_7	$3.523\,64 \times 10^{-7}$	$-1.292\,65 \times 10^{-7}$	63.315

harmonic model has the hardest time recreating the odd zonal harmonics, specifically J_5, which could be due to the fact that the odd zonal harmonics are not symmetric about the equator causing the model to have a harder time matching their sign. This is could also be attributed to very small numerical error due to the level of precision of the coefficients. All magnitudes of the derived zonal harmonics match though.

Figure 4.16 shows the acceleration error for various truncation degrees on all ten Brillouin spheres. Across each sphere, the errors from each truncation point only differ by $\sim 10^{-4}$. This shows that the choice of a truncation degree does not have a strong effect on the error in the acceleration field.

Orbital Parameters

Figures 4.17 and 4.18 show the time evolution of the orbital parameters using R_1/r and R_{10}/r respectively. The choice of Brillouin sphere radius has minimal impact on the output orbital parameters. The inclination using R_{10}/r is 1.00006 times more accurate than the inclination output from R_1/r, the eccentricity derived from radius R_1/r is 1.002 times more accurate than R_{10}/r, and finally the specific angular momentum derived from R_1/r is 1.0007 times more accurate than that from R_{10}/r.

For the case of a larger orbital radius such as the inclined orbit shown here, the large perturbations in the gravitational field are greatly dampened and cause little turmoil in

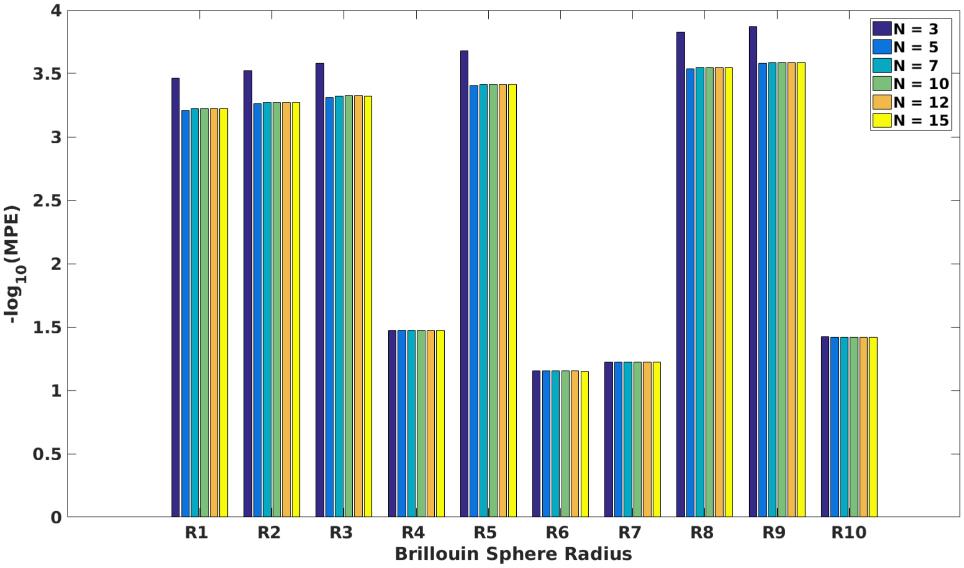

Figure 4.16: The -$\log_{10}$ *of the mean percent difference in the acceleration field derived from the theoretical zonal harmonics of Earth and the spherical harmonic model on each Brillouin sphere for truncation degrees* $N = 3, 5, 7, 10, 12$ *and 15.*

the choice of a Brillouin sphere radius and truncation degree of the harmonic series. If this model is being used for an orbit such as this one, it is recommended that the smallest Brillouin sphere ($R_S/r = 5\%$) be used with a truncation degree of either N = 8 or 15 based upon the error in the potential field (Figure 4.14).

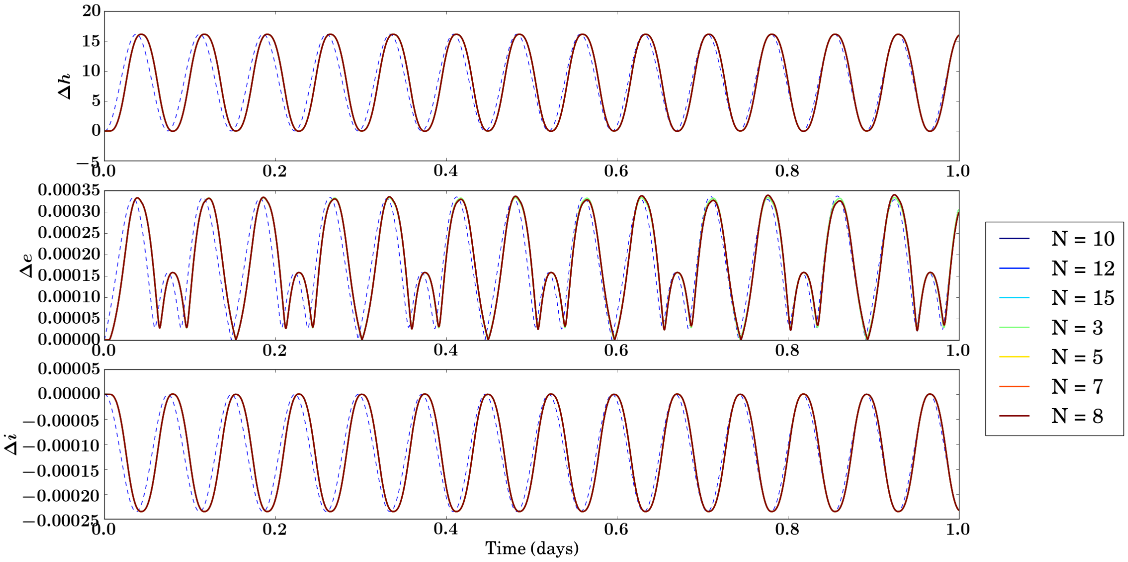

Figure 4.17: Comparison of the change in the time evolution of orbital parameters for an inclined orbit. The dashed line shows the "true" output and the colored lines are derived from various truncation degrees of the spherical harmonic series. A Brillouin sphere radius of $R_S/r = 5\%$ was used.

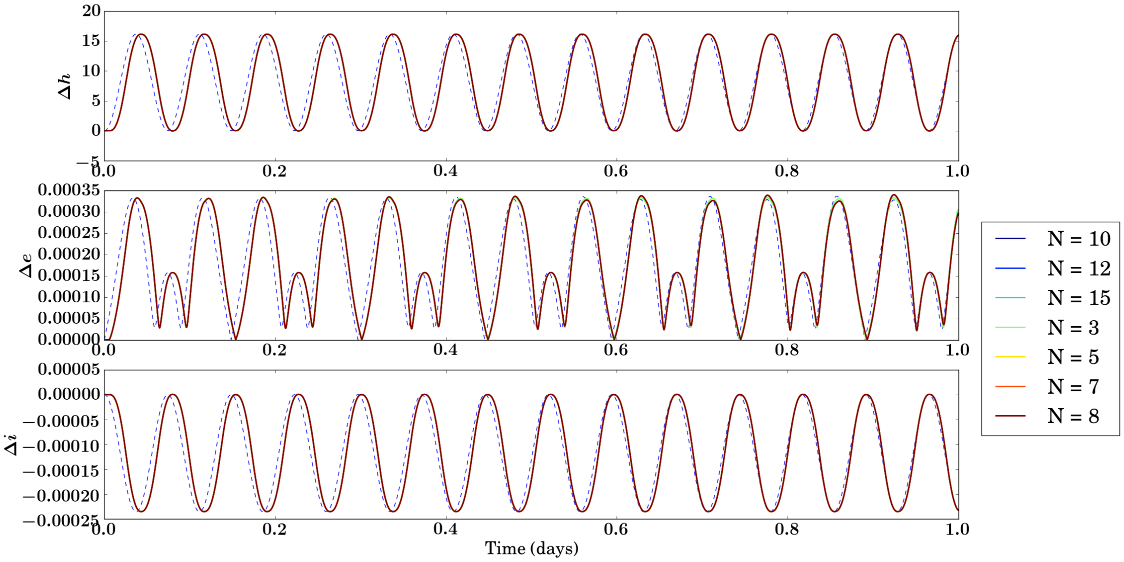

Figure 4.18: Comparison of the change in the time evolution of orbital parameters for an inclined orbit. The dashed line shows the "true" output and the colored lines are derived from various truncation degrees of the spherical harmonic series. A Brillouin sphere radius of $R_S/r = 95\%$ was used.

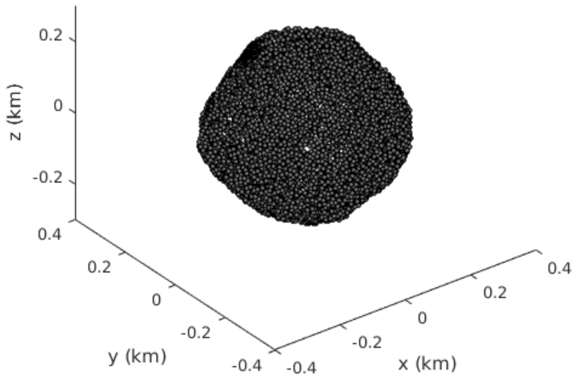

Figure 4.19: Reconstruction of Asteroid 101955 Bennu using a mascon distribution of the body.

Asteroid 101955 Bennu

Two orbits around asteroid 101955 Bennu are simulated using a mascon model of the body and the spherical harmonic model. The first orbit is a low orbit (LO) of altitude $r = 0.5$ km and the second is a medium orbit (MO) with altitude $r = 2.0$ km. Bennu is ~ 0.5 km in diameter, so it's gravity field is relatively weak compared to that of Earth's and the dynamics around such a small body are very different. Bennu's largest perturbation is a J_2 perturbation which can be seen as the bulge at Bennu's equator (Figure 4.19).

In the previous section, it was determined that a Brillouin sphere radius of 95% of the orbital altitude gave the most accurate results compared to the smaller radii. Therefore, that radius will be used to analyze orbits about Bennu. A sample of the derived series coefficients are listed in Appendix B.

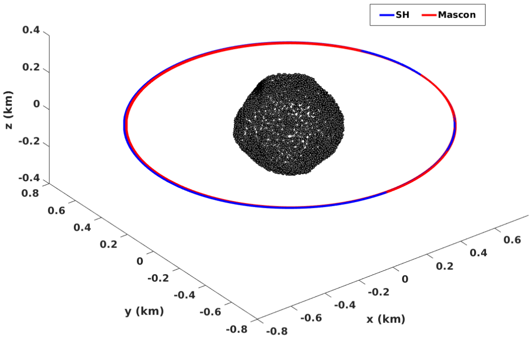

Figure 4.20: LO with altitude of 0.5 km. The mascon derived output is in red and the spherical harmonic model output is in blue.

LO

Figure 4.20 gives a qualitative comparison of the output trajectories from a mascon model of Bennu and a spherical harmonic model. Visually there is a good overlap between the two model outputs.

Looking at the time evolution of the orbital parameters for this trajectory (Figure 4.20), it is seen that the dynamics of the orbit are never quite met, but after a point, there is a convergence of the spherical harmonic output. This shows that the error in the harmonic derived parameters goes to zero as the truncation degree of the series increases which is what is expected of a converging series.

While the mascon and spherical harmonic derived parameters never match, the differences between the two are on the order of 10^{-1}, 10^{-2}, 10^{-3} for h, e, and i respectively. This level of precision is high enough where it would not cause an issue for an orbiting spacecraft that is using the spherical harmonic model to conduct maneuvers.

To get a better idea of the differences in the orbital parameter output, Figure 4.22 shows the time evolution of just the inclination for both models using only N = 3, 5, 7, and 15. It

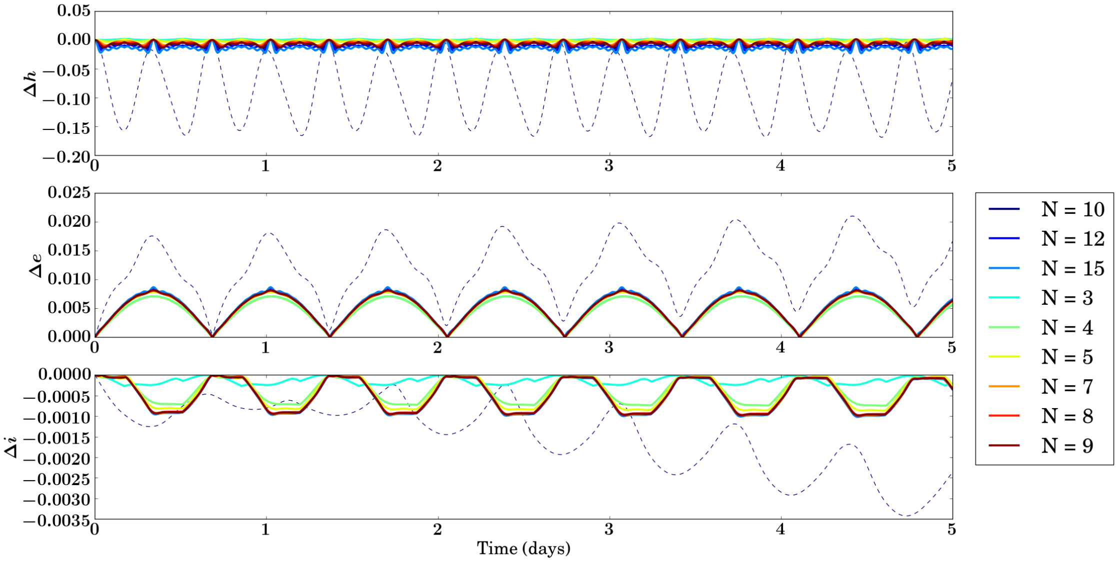

Figure 4.21: Comparison of the change in time evolution of orbital parameters of a LO orbit about asteroid Bennu. The dashed line shows the mason model derived parameters and the colored lines are derived from various truncation degrees of the spherical harmonic model.

is quickly seen that N = 3 does not do a good job at modeling the inclination. N = 5 gives a more accurate output compared to N = 3, but it is still $\sim 10^{-3}$ off of the mascon output. N = 15 and 7 give almost identical outputs where the ratio of their errors is ∼0.991. Based on this, a truncation degree of N = 7 is reasonable to use for further simulations.

Figure 4.23 shows the gravitational potential field on the Brillouin sphere used for this orbit (top) compared to the "true" (mascon derived) potential field (bottom). There is a $7.05 \times 10^{-4}\%$ difference between the two fields when using N = 7.

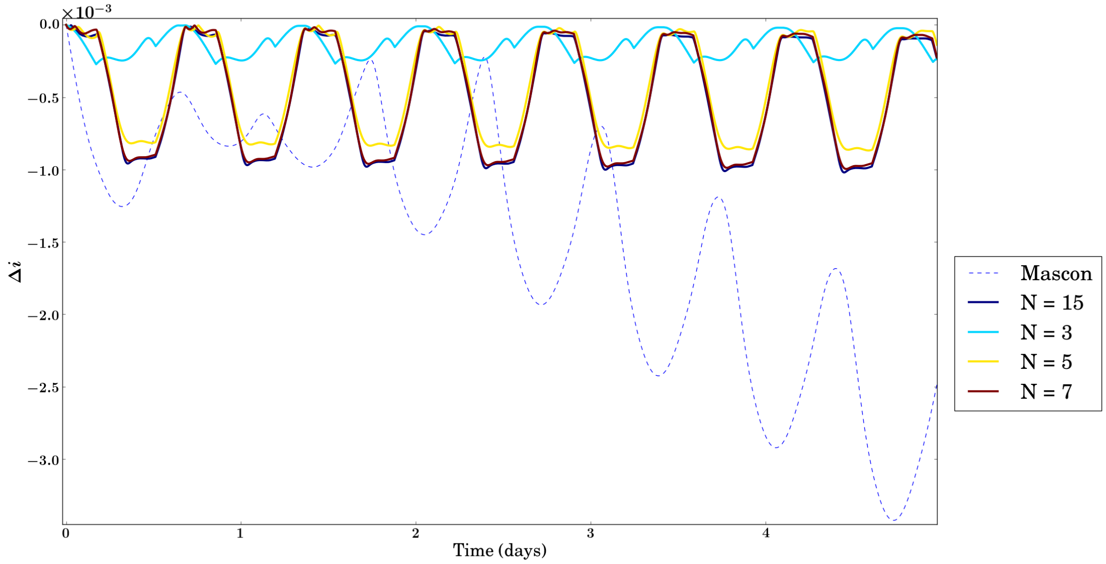

Figure 4.22: Comparison of the change in time evolution of the inclination of a LO orbit about asteroid Bennu. The dashed line shows the mascon model output and the colored lines are derived from the spherical harmonic model using N = 3, 5, 7, 15.

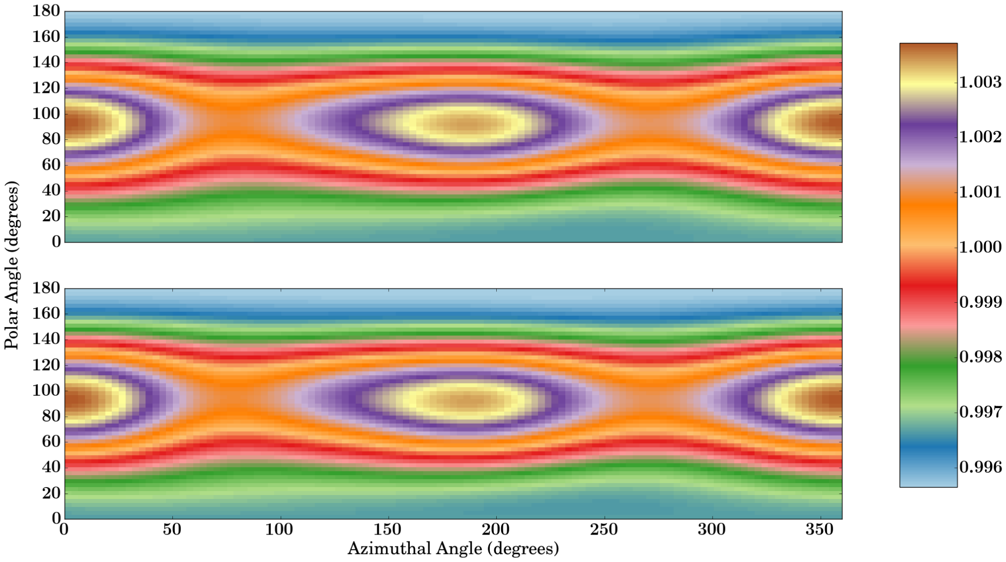

Figure 4.23: Comparison between the gravitational potential field of asteroid Bennu at $R_S/r = 95\%$ *derived from the mascon distribution model (bottom) and spherical harmonic model (top) using* $N = 7$.

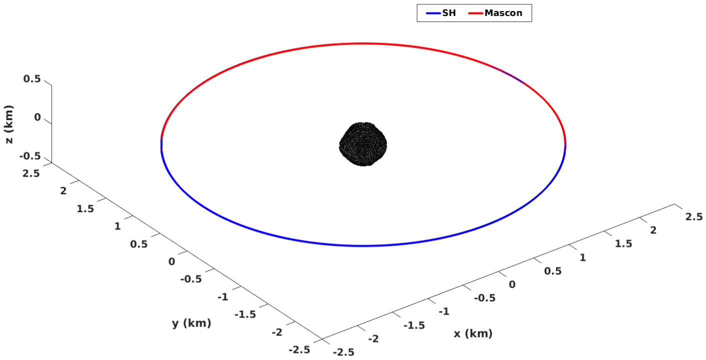

Figure 4.24: MO with altitude of 2.0 km. The mascon derived output is in red and the spherical harmonic model output is in blue.

MO

The orbital altitude is now increased to 2 km above the surface of Bennu. The spherical harmonic model and the mascon distribution model output line up well as seen in Figure 4.24 where the blue trajectory is derived from the harmonic model and the red from the mascon model.

Figure 4.25 quantitatively compares the two MO orbits by looking at the change in the time evolution of the orbit's parameters. The dynamics in the specific angular momentum (h) and the eccentricity (e) are mirrored between the two models, but the harmonic output cannot quite match the amplitude of each parameter. The mean difference in h between both models is $\sim 5 \times 10^{-3}$ and $\sim 5 \times 10^{-4}$ for e. After about N = 5, the harmonic derived parameters converge upon each other for each of these parameters.

For the case of the change in inclination (i) though, the harmonic model output has a harder time matching the mascon output. Figure 4.26 shows the time evolution of the inclination alone for an extended number of truncation degrees (N = 5 - 50). Increasing the truncation degree from N = 5 to N = 20 gives a slight increase in accuracy for the

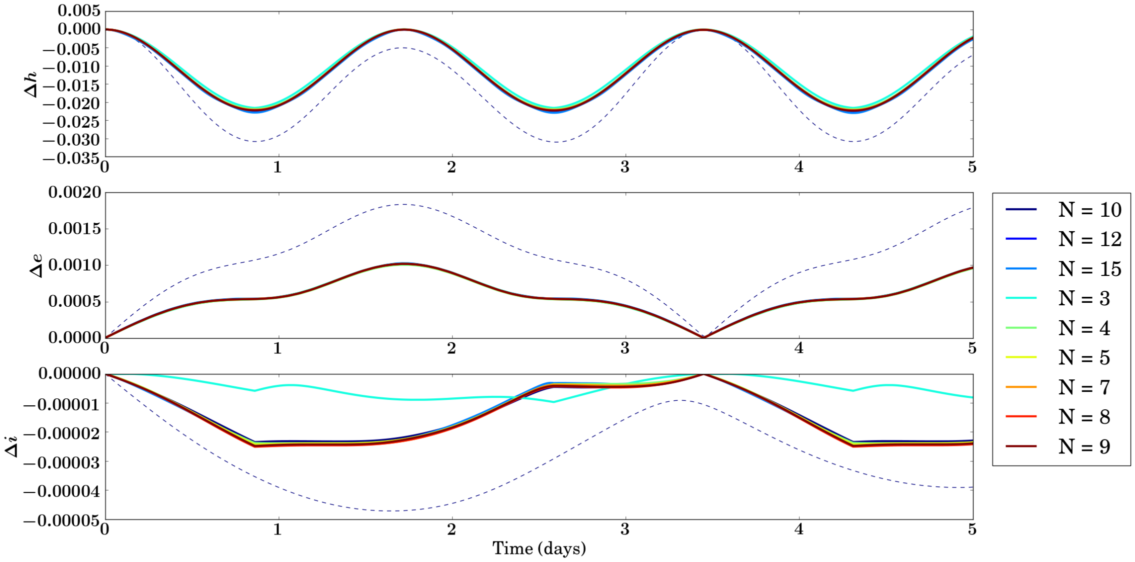

Figure 4.25: Comparison of the change in time evolution of orbital parameters of a MO orbit about asteroid Bennu. The dashed line shows the mason model derived parameters and the colored lines are derived from various truncation degrees of the spherical harmonic model.

inclination, but after N = 20, small oscillations appear in the data. This noise can be attributed to numerical error based on the high precision of the coefficients being used in these calculations ($\{C_n^m, S_n^m | \forall n \geq 30, \forall m = 0, ..., n\}$). Each curve gives a mean difference error of $\sim 1 \times 10^{-5}$ where N = 30 gives the lowest mean difference error of 1.47×10^{-5}.

Based on the errors seen in all orbital parameters, a truncation degree of N = 5 will offer a reasonable trade-off between the run-time of the simulation and the accuracy of the output. Although N = 30 gave the lowest mean difference error in the inclination output, the difference between N = 5 and N = 30 is essentially negligible ($\sim 6 \times 10^{-7}$) which allows for the choice of N = 5 in the overall calculations.

Figure 4.27 shows the gravitational potential field on the Brillouin sphere used for this orbit (top) compared to the "true" (mascon derived) potential field (bottom). There is a $1.04 \times 10^{-3}\%$ difference between the two fields when using N = 5.

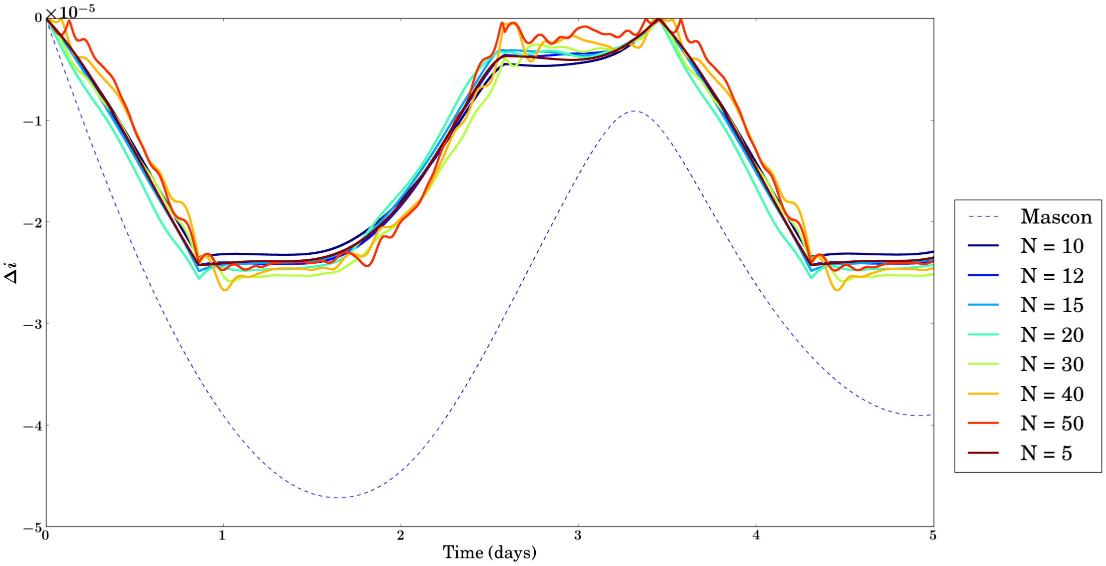

Figure 4.26: Comparison of the change in the time evolution of the inclination of a MO orbit about asteroid Bennu. The dashed line shows the mascon model output and the colored lines are derived from the spherical harmonic model using N = 10, 15, 20, 30, 40 and 50.

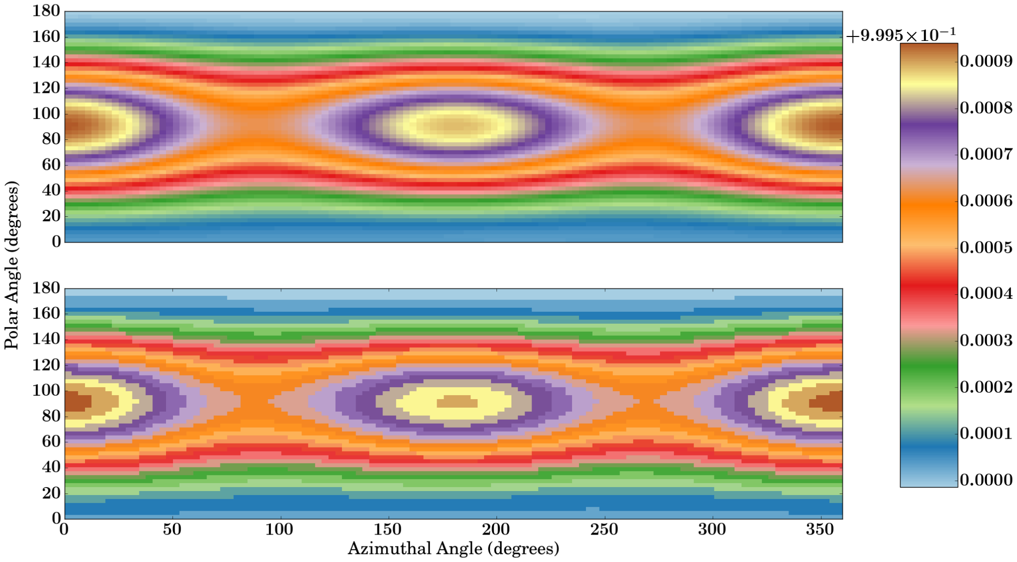

Figure 4.27: Comparison between the gravitational potential field of asteroid Bennu at $R_S/r = 95\%$ derived from the mascon distribution model (bottom) and spherical harmonic model (top) using $N = 5$.

CHAPTER 5

MODELING CONTACT BINARIES

The spherical harmonic model was shown to accurately model homogeneous density bodies in the previous chapter, but in reality, asteroids and comets will not be of one density and a useful gravity model will need to be able to handle such variances.

Asteroid 25143 Itokawa was the subject of JAXA's *Hayabusa* mission in 2003. From data taken by the *Hayabusa* orbiter, it was determined that Itokawa is composed of two densities at the least [26]. Itokawa is used as the test case for the variable density adaptation of the model presented in this thesis.

ASTEROID 25143 ITOKAWA

The spherical harmonic model is implemented in several steps: (1) The gravitational potential is calculated from the mascon distribution of the body, (2) This potential is projected onto a Brillouin sphere, (3) The spherical harmonic series coefficients for the field are calculated, and (4) The acceleration field at a user defined radius is calculated and a trajectory is output. The impacts of each of these steps will be discussed in relation to the dual-density mascon model of Asteroid Itokawa which is assumed to be the true model of the asteroid. For the sake of comparison, a rotational spherical harmonic potential field is not

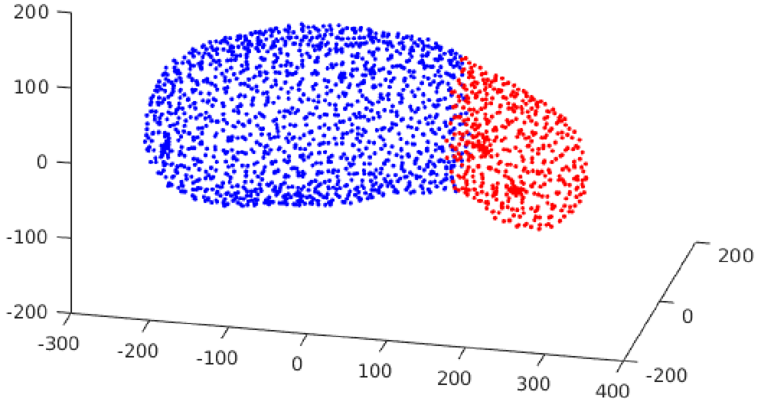

Figure 5.1: Variable density subsections of asteroid Itokawa. The body (blue) has a lower density than that of the head (red).

implemented in the following results.

Mascon

Itokawa is modeled using mascons of variable volume (see Appendix A) to approximate the true shape of the asteroid with a high precision. A polyhedral-dual mesh containing ~15,000 elements was used in the calculations for the entire asteroid and ~4,400 and 11,000 cell meshes were used for the individual head and body reconstructions of Itokawa. A uniform density model of Itokawa is examined prior to a dual-density model to discern the perturbations induced by this body on a spacecraft from its geometry alone. Two trajectories were chosen to analyze this behavior, an inclined orbit and an equatorial orbit.

Uniform Density

To illustrate the dynamical environment around asteroid Itokawa, two orbital trajectories are examined using Itokawa's bulk density ($\rho = 1950\ kg/m^3$) and rotational rate of $\omega = 1.4386 \times 10^{-4}$ rad/s about it's z-axis. Figure 5.2a shows the trajectory of an orbit inclined to the plane of rotation of Itokawa (i $\approx 50°$) and Figure 5.3a shows the evolution of a body orbiting initially in the plane of rotation. Both trajectories are simulated for 10 days. Itokawa is rotating about it's z-axis and has a period of 12.13 hours [27]. The time evolution of the orbital parameters are shown in Figure 5.3.

Although both trajectories are simulated for the same amount of time, the dynamics of the equatorial orbit are more pronounced than those of the inclined orbit. As seen in Figure 5.3b, the eccentricity quickly deviates from circular as the orbiting spacecraft experiences a slight increase in elevation and angular momentum throughout its orbit. Both trajectories show an orbital resonance throughout the entire duration of the orbits. This pattern is indicative of a smoothing of the gravitational perturbations induced by Itokawa.

Dual-Density

The dynamics seen in trajectories about Itokawa are heightened in the dual-density model. As the spacecraft passes the "body" of Itokawa, the radius of the orbit increases (Figure 5.4a). This can be attributed to the lower density in this region compared to that of the "head" of Itokawa.

Figure 5.4b shows the differences in the time variation in the orbital parameters derived from the uniform (blue) and dual-density (red) models of asteroid Itokawa. The variations in the parameters are much more pronounced for the dual-density model.

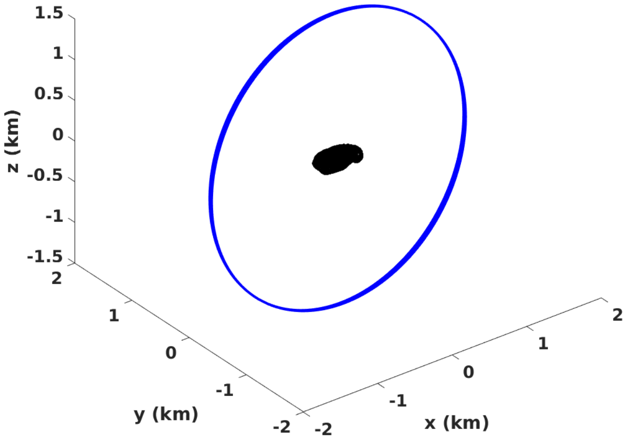

(a) Inclined Orbit

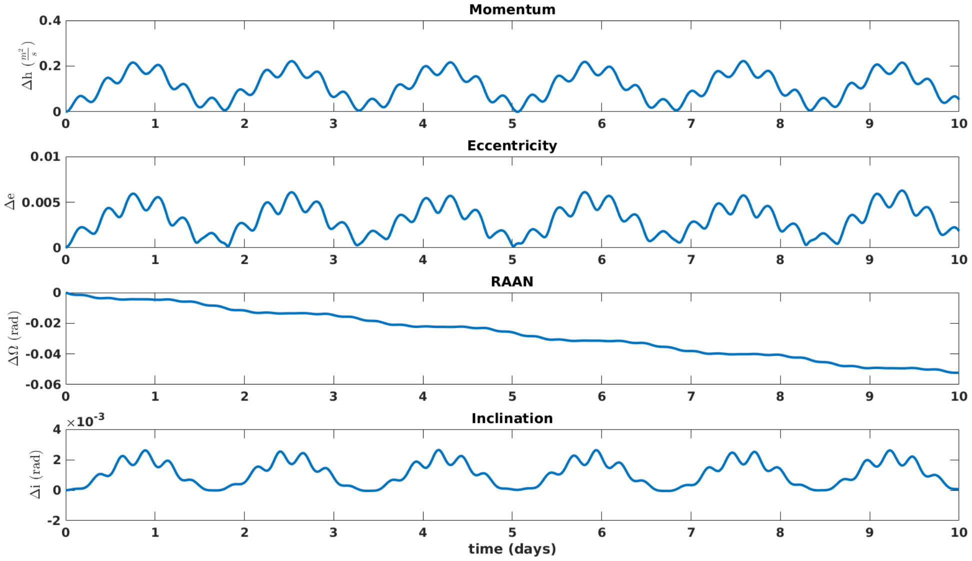

(b) Inclined Orbital Parameters

Figure 5.2: Inclined orbit about Asteroid 25143 Itokawa and corresponding change in time evolution of orbital parameters. A non-uniform mascon distribution model with homogeneous density was used. The orbital parameters shown are, the specific angular momentum, eccentricity, right ascension of the ascending node (RAAN), and inclination of the orbit.

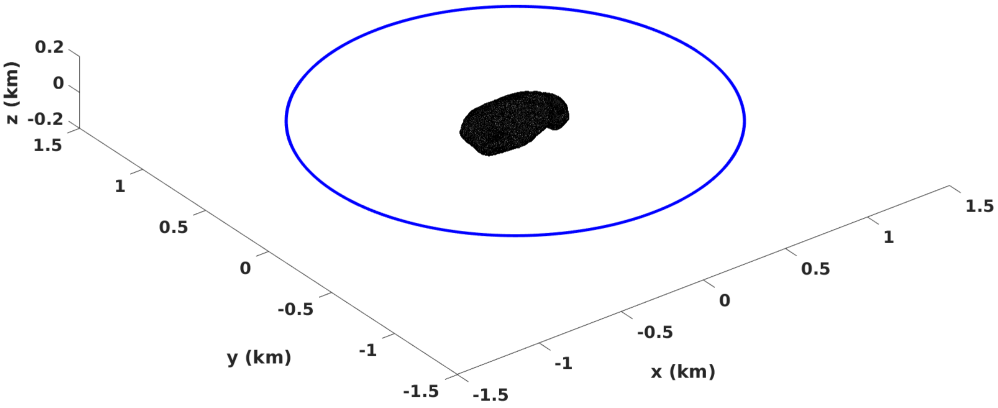

(a) XY-Planar Orbit

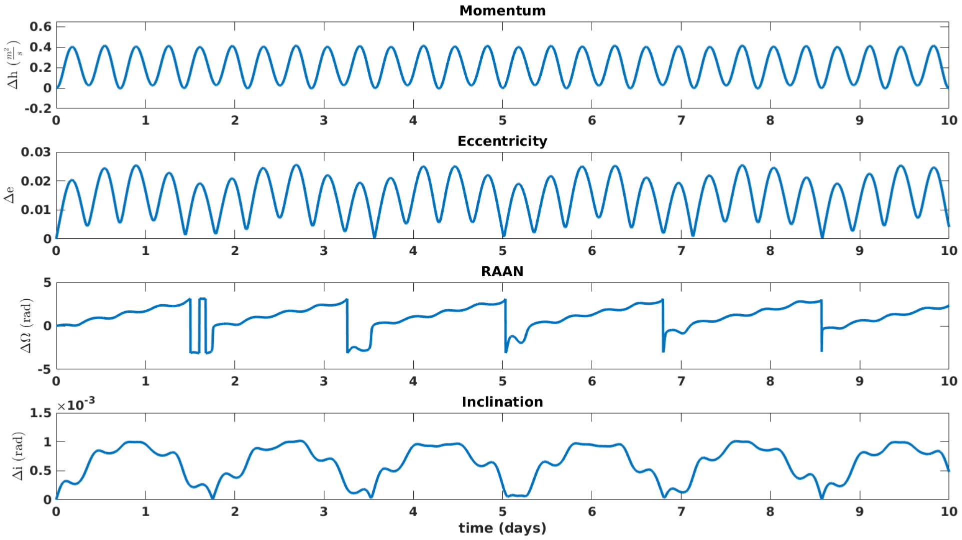

(b) XY-Planar Orbital Parameters

Figure 5.3: Equatorial orbit about Asteroid 25143 Itokawa and corresponding change in time evolution of orbital parameters. A non-uniform mascon distribution model with homogeneous density was used. The orbital parameters shown are, the specific angular momentum, eccentricity, right ascension of the ascending node (RAAN), and inclination of the orbit.

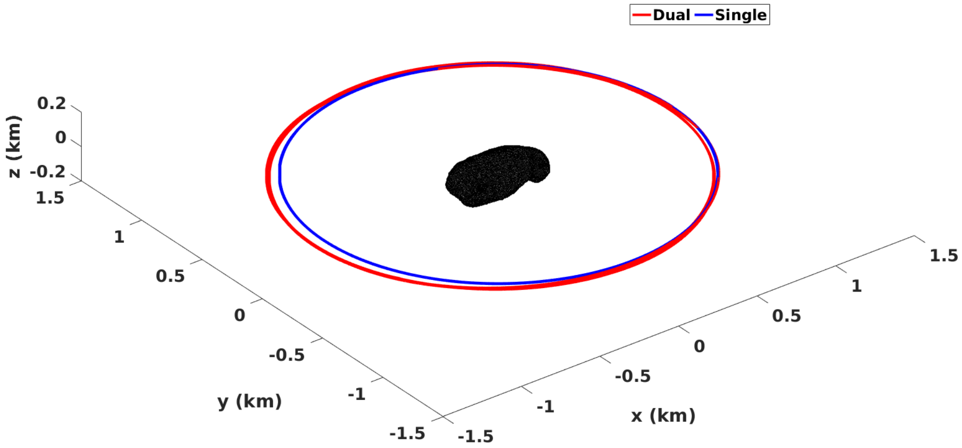

(a) XY-Planar Orbit

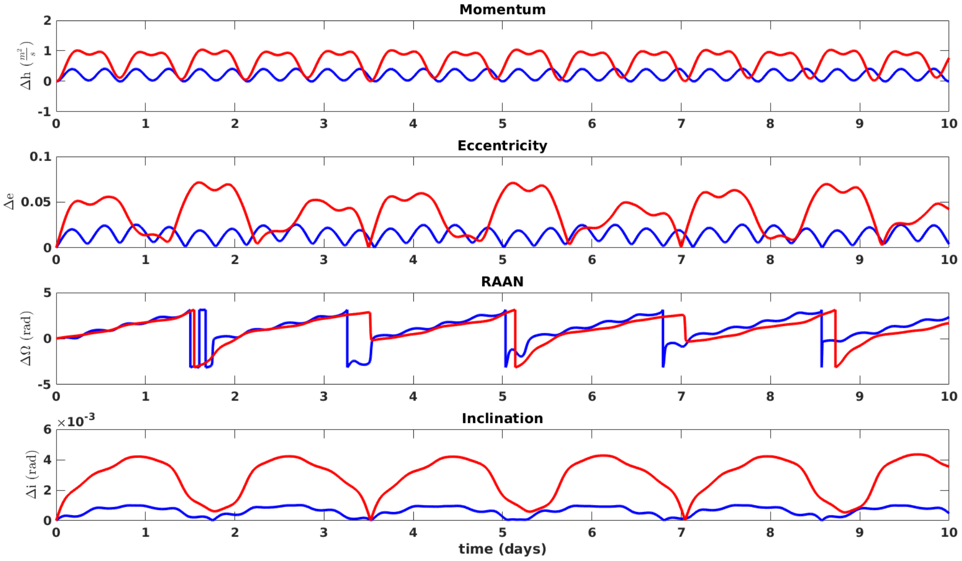

(b) XY-Planar Orbital Parameters

Figure 5.4: Equatorial orbit about Asteroid 25143 Itokawa and corresponding change in time evolution of orbital parameters simulated for ten days. The red path is derived using the dual-density model and the blue from a homogeneous density equal to the bulk density of Itokawa.

IMPACT OF BRILLOUIN SPHERE RADIUS

The same two test case trajectories as were used in the mascon distribution analysis (an equatorial orbit and an inclined orbit) were chosen to analyze the effects and behavior of variable radii Brillouin spheres. The Brillouin sphere radii were varied between 5% and 95% of the orbital altitude as with Earth and asteroid Bennu. This technique is used for both the head and the body of Itokawa, so there is an overlap between the two Brillouin spheres of both subsections of the asteroid (Figure 5.5).

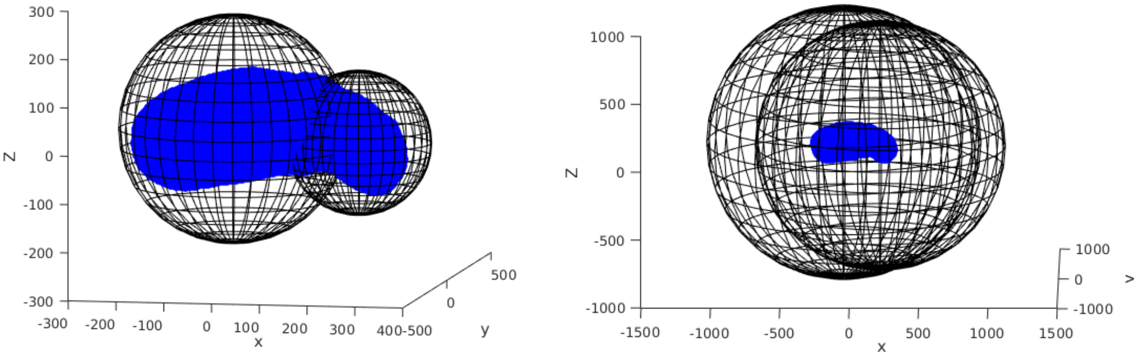

(a) $R_s/r = 5\%$

(b) $R_s/r = 95\%$

Figure 5.5: Example of how the Brillouin spheres centered on the head and body of Itokawa can overlap when large enough.

Figure 5.6 compares the average error in the acceleration field in both the two (blue triangles) and single (red circles) Brillouin sphere models. Both of these models utilize a dual-density mascon distribution, so the only difference is the way the acceleration field is calculated from each Brillouin sphere; a piecewise manner for the two spheres and a direct implementation of Eq. 3.4 for the single sphere. The truncation degree of the series was held constant at N = 7 for sake of comparison of the Brillouin spheres alone. By using two spheres, the error in the acceleration field is greatly decreased. At $R_1/r = 5\%$ the error is decreased by a factor of 3 and at $R_{10}/r = 95\%$, a factor of 11. Bisecting the

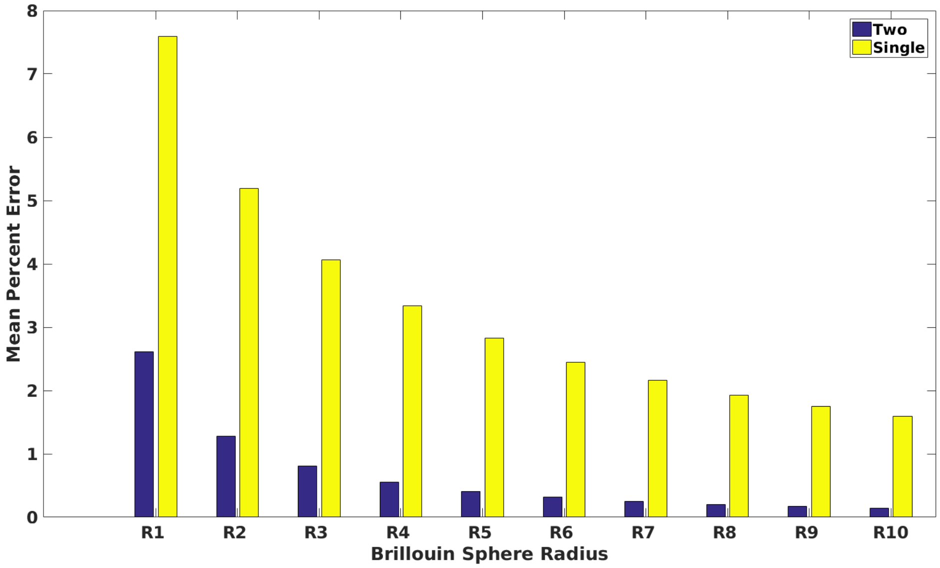

Figure 5.6: Mean percent difference in the acceleration field averaged over each Brillouin sphere. The acceleration error was calculated using a single Brillouin sphere (yellow) and two Brillouin spheres (purple).

body of Itokawa results in two sections that are more spherical than ellipsoidal allowing the spherical harmonic series expansion of both subsections to more accurately model the true environment of the body.

Since it was determined that using two Brillouin spheres around the homogeneous density subsections of Itokawa is more accurate than one, the radii of the spheres must be determined. Holding the degree of the spherical harmonic series constant, the error in the acceleration field decreases as the Brillouin sphere radii (in the two Brillouin sphere model) are increased from 5% to 95% of the orbital altitude when compared with the dual-density mascon model (Figure 5.7). Acceleration errors on Brillouin spheres derived from both an equatorial orbit and an inclined orbit are shown in Figure 5.7 and show the same decreasing trend as the sphere's radius is increased. This is expected as the perturbations induced by the asteroid are dampened as the distance from its surface is increased (due to the $1/r^2$ dependence of the acceleration field). For the remainder of this analysis, acceleration errors in the inclined orbit will be used because of the similar outcomes between the two orbits and for sake of redundancy. The inclined orbit, as opposed to the equatorial orbit, will be used because it has a larger orbital altitude thus rendering the Brillouin sphere range R_s/r larger and easier to discern on a figure.

These results indicate that the largest Brillouin sphere radius, R_{10}/r gives the most accurate output when calculating orbital trajectories.

IMPACT OF SERIES TRUNCATION

The degree of truncation will be chosen and analyzed in the same manner that the Brillouin sphere radius was; via acceleration field error. It was seen in the previous section that the largest Brillouin sphere gave the most accurate output for a given trajectory. This result now needs to be proved in-line with multiple truncation degrees to show that it is not an artifact of one specific truncation degree of the series.

Truncation degree and Brillouin sphere radii were allowed to vary in order to determine a spatial location that will give an accurate trajectory while not requiring an excessive computational run-time. Truncation degrees of N = 3, 7, 15, and 30 were used to compare the error in the acceleration field (Figure 5.8) between the dual-density mascon model and the spherical harmonic model.

Figure 5.8 shows the same decrease in error as the Brillouin sphere radii are increased that was seen in Figure 5.7, but now it shows a convergence of the error across increasing truncation degrees as well. For the smallest Brillouin sphere radius ($R_1/r = 5\% \approx 375m$), N = 30 (blue) and N = 3 (red) give slightly higher errors than N = 7 (yellow) and N = 15 (green). Because this is the closest point to the body, a larger truncation degree is necessary to accurately model the dynamics of the environment. A degree of N = 7 allows for this. It was expected that the error in the acceleration field would scale with the truncation degree of the spherical harmonic series, but as seen in the case of R_1, this is not true. N = 30

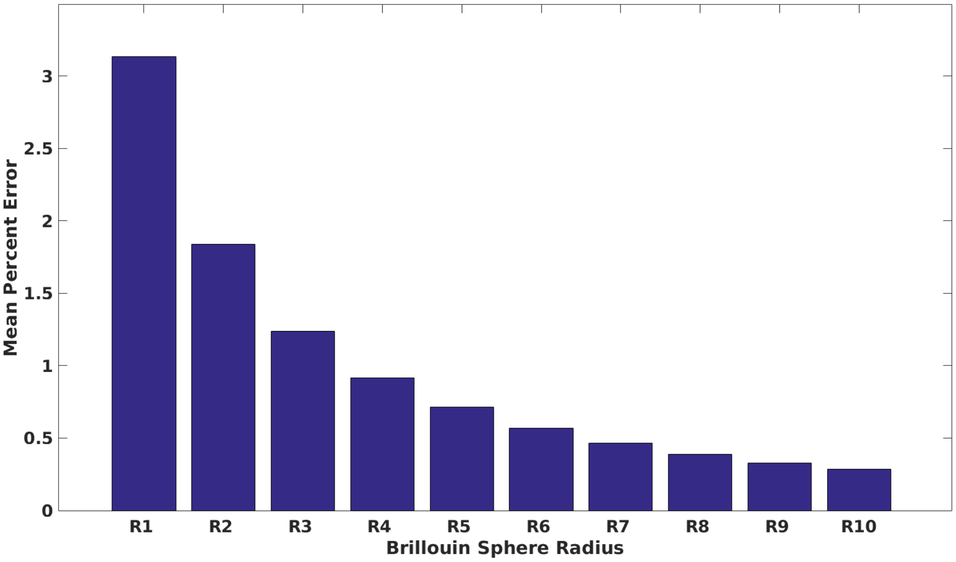

(a) Equatorial orbit.

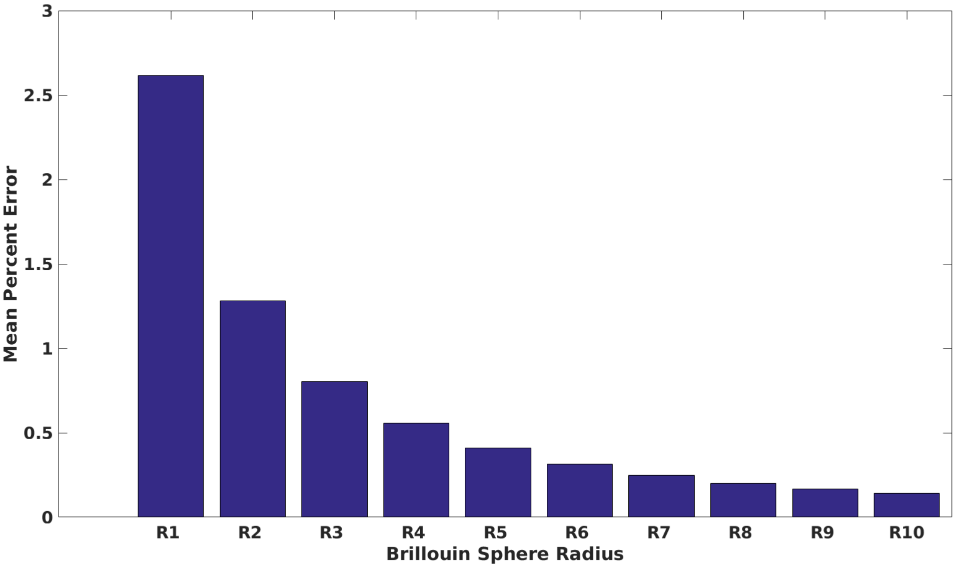

(b) Inclined orbit.

Figure 5.7: Mean percent difference in the acceleration field averaged over each Brillouin sphere for a constant spherical harmonic series truncation degree.

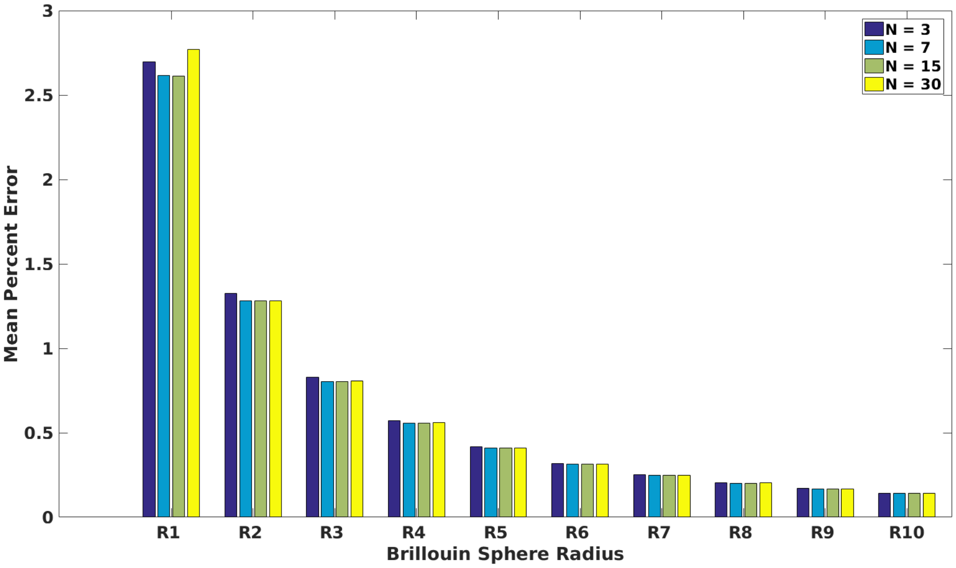

Figure 5.8: Mean percent difference in the acceleration field averaged over each Brillouin sphere for all truncation degrees of the spherical harmonic series. Each color is indicative of a Brillouin sphere radius and each symbol a truncation degree.

results in a larger error in the acceleration field than the lower truncation degrees at 7 and 15. This discrepancy is attributed to numerical error incurred throughout the simulation and a non-monotonic convergence of the spherical harmonic series.

As the Brillouin sphere is increased to R_{10} ($95\% * r \approx 1500m$), the error in the truncation point of the series converges due to the increased distance from the surface of the body. By comparing all ten Brillouin sphere sizes for each of the four truncation points, it is seen that the largest Brillouin sphere radius ($R_s/r = 95\%$) gives the most accurate output and a truncation degree of N = 7 will result in an acceleration field with minimal error incurred and a lower simulation run-time.

For the remainder of this analysis, a Brillouin sphere of $R_s/r = 95\%$ and a truncation point of N = 7 will be used.

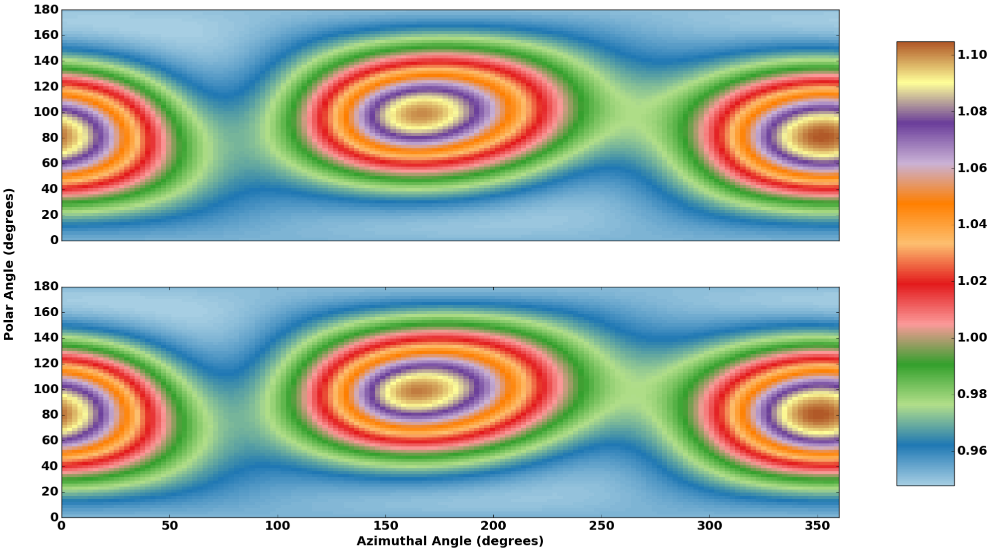

Figure 5.9: Comparison between the "true" gravitational potential field of the body of Itokawa (bottom) and the spherical harmonic reconstruction of the field (top).

Gravity Field Matching

With the radius of the Brillouin sphere and the truncation degree of the series chosen, the potential field can be calculated. The potential field of the head of Itokawa (Figure 5.10) has a $7.9 \times 10^{-4}\%$ mean difference and the body (Figure 5.9) has a $2.3 \times 10^{-3}\%$ mean difference between the mascon derived and the spherical harmonic derived field. Whereas the field of the entire asteroid (Figure 5.11) has a $3.6 \times 10^{-3}\%$ mean difference between the two fields.

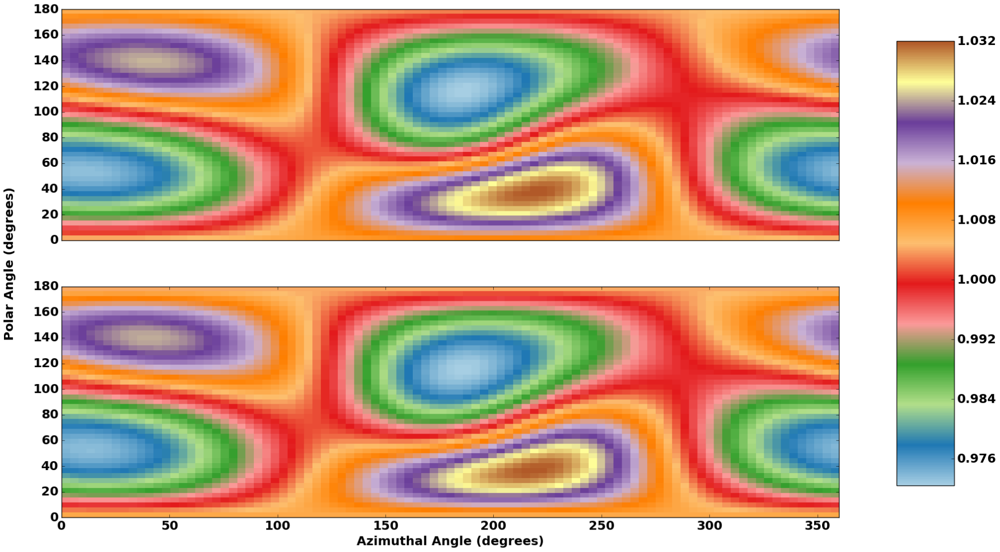

Figure 5.10: Comparison between the "true" gravitational potential field of the head of Itokawa (bottom) and the spherical harmonic reconstruction of the field (top).

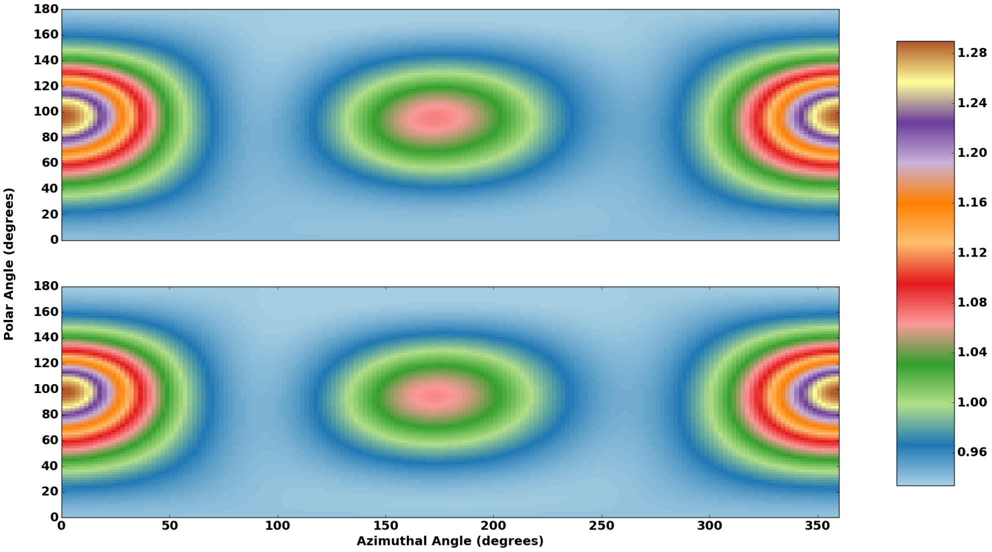

Figure 5.11: Comparison between the "true" gravitational potential field of the entirety of Itokawa (bottom) and the spherical harmonic reconstruction of the field (top).

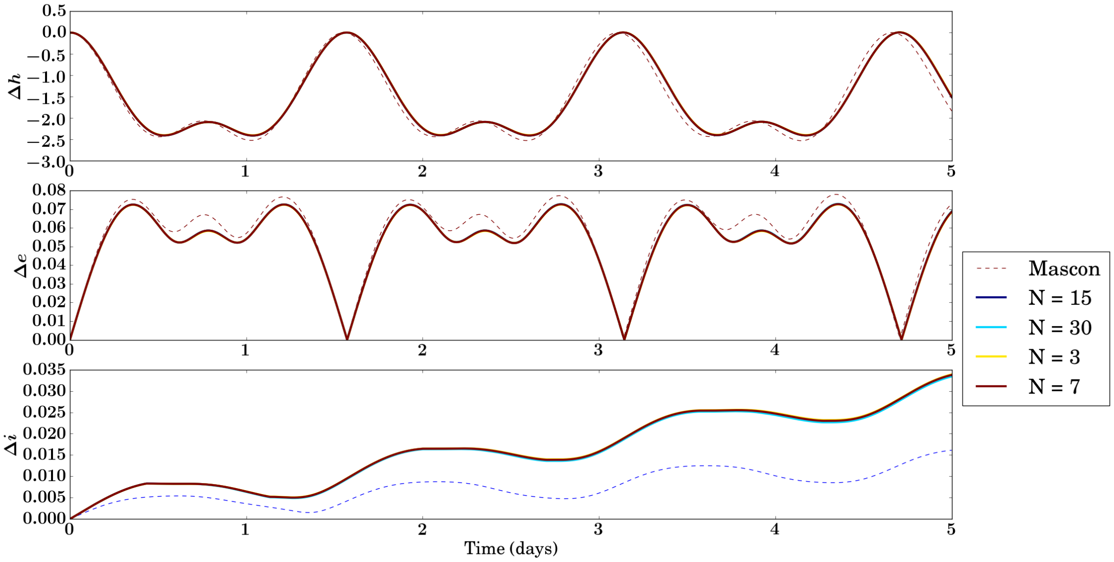

Figure 5.12: Time evolution of orbital parameters for an equatorial orbit about asteroid Itokawa using a Brillouin sphere that is 95% of the orbital altitude. Four truncation points of the spherical harmonic series are shown in comparison to the mascon distribution derived output.

Orbital Parameters

The resulting orbital parameters for an equatorial and inclined orbit using the R_{10}/r radius Brillouin sphere for both subsections of Itokawa are shown in Figures 5.12 and 5.13 respectively. All of the test-case truncation degrees (N = 3, 7, 15, and 30) are plotted here for sake of comparison.

There is a $\sim 10^{-2}\%$ mean difference between the N = 3 and N = 30 outputs and a $\sim 10^{-3}\%$ mean difference between the N = 7 and N = 15 outputs. While there is a greater accuracy seen when a larger truncation point is used, the trade-off between the run-time of the simulation and the accuracy of the output must be considered. Also, the decreasing nature of the mean difference between outputs from differing truncation points implies a convergence of the results. This convergence is easily seen in Figures 5.12 and 5.13 and the small discrepancies between the mascon and the spherical harmonic outputs are small enough to ideally not cause problems for a spacecraft conducting maneuvers based upon this model. The minute differences between the varying truncation degrees in the output orbital parameters again show that the choice of N = 7 is a reasonable choice for these orbital trajectory simulations.

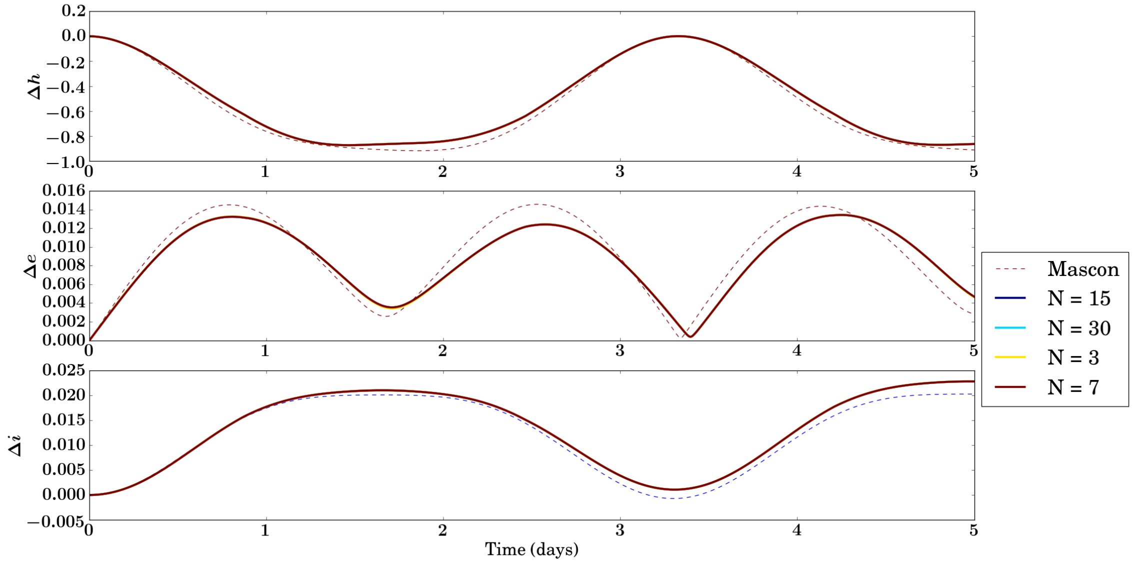

Figure 5.13: Time evolution of orbital parameters for an orbit inclined to the equatorial plane of asteroid Itokawa using a Brillouin sphere that is 95% of the orbital altitude. Four truncation points of the spherical harmonic series are shown in comparison to the mascon distribution derived output.

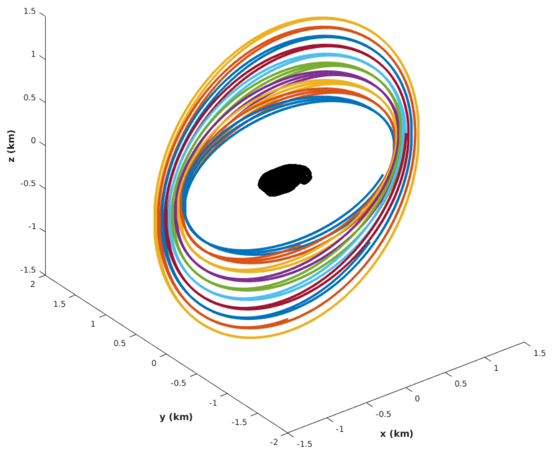

Figure 5.14: Various orbits about Asteroid Itokawa used to analyze the dynamics at differing inclinations.

Impact of Orbital Inclination

A higher mean percent difference error was seen in the equatorial orbit around Itokawa compared to the inclined orbit. This leads to the hypothesis that there is a region around Itokawa with greater dynamics than others or a region where the spherical harmonic model has a harder time modeling the dynamical field than others. This is a reasonable hypothesis due to the shape of the body. Itokawa is smoother on its top side and has an indent/canyon on its underbelly which is referred to as the “neck” of Itokawa. These varying topologies give rise to a range of dynamics in orbits with differing inclinations.

To analyze this behavior, a range of inclinations were swept through (Figure 5.14) and the mean percent difference errors in the orbital parameters derived from the dual-density mascon model and two Brillouin sphere spherical harmonic model were compared (Table 5.1). The inclinations range from just above the equatorial plane ($i = 7.125°$) to an almost polar orbit ($i = 87.138°$).

Table 5.1: Mean differences between the "true" and harmonic model derived change in evolution of orbital parameters for various inclinations.

Inclination (deg)	**Mean Percent Difference (%)**		
	h	e	i
7.1250	7.52301	0.41427	0.15134
14.036	21.78982	1.28696	0.24433
20.556	41.53408	2.55221	0.52005
26.565	47.73416	7.31852	0.65689
32.005	53.93051	13.84161	0.79992
36.870	52.21836	19.02342	0.88931
41.186	45.25302	25.56024	0.83164
45.000	33.82501	37.87304	0.66338
48.366	31.08779	45.43295	0.64487
51.340	3.07804	0.11698	0.10563
87.138	0.19687	0.04018	0.00141

The error in all of the orbital parameters increases up to a point and then start to decrease. The specific angular momentum (h) and inclination (i) errors increase until $i = 36.87°$ whereas the error in the eccentricity (e) continues to increase until $i = 48.366°$ then dramatically drop at $i = 51.34°$ with the other parameters. The spherical harmonic model seems to have an easier time matching the dynamics of the trajectory after $i \approx 50°$ (the inclination analyzed in the previous sections). At lower inclinations, as the spacecraft moves around Itokawa, it is going to "see" more of the asteroid which means it will experience more of the perturbations in the gravity field. As the inclination of the orbit increases to $i = 90°$, the spacecraft's field of view of Itokawa reduces to its nadir and thus much less of the asteroid is seen. The gravitational perturbations induced on a spacecraft are greatest at or just above Itokawa's equator because the spacecraft is "seeing" most of the body during these orbits. At higher inclinations, the orbiting spacecraft is enduring minimal perturbative forces from the body and thus the spherical harmonic model can more easily model the trajectory.

CHAPTER 6

CONCLUSIONS

Missions to small, celestial bodies demand autonomy and with a rise in interest for these types of missions, the demand for high-fidelity modeling techniques has increased. These modeling techniques must expand upon the dubious nature of comets and asteroids to allow for successful mission planning.

This thesis focused on the characterization of a spherical harmonic based model that used a mascon distribution of a body as its boundary conditions for the potential field. This model was then used to model the dynamic environment of contact binaries. Three bodies of varying geographical asymmetries were used to quantify the utility of this model for homogeneous and dual-density bodies. Errors in the gravity and acceleration fields were analyzed over multiple trajectories about each body and it was found that the error incurred in the final simulated trajectory can be decreased by varying the radius of the Brillouin sphere and the truncation point of the harmonic series.

By varying the radius of the Brillouin sphere, it was found that a Brillouin sphere that is closest to a given orbit will give the most accurate results. A serendipitous consequence of using a larger Brillouin sphere is that less terms in the spherical harmonic series expansion are needed since the perturbations induced by the body are dampened as the distance from the body's surface increases. Fewer terms in the series expansion offers a computational speed-up of orbital trajectory simulations about the body.

The precision of the spherical harmonic model presented was characterized by the backwards computation of the potential field of Earth. The potential field was found with a relative accuracy of $\sim 10^{-6}$ using a truncation point of N = 8 and a Brillouin sphere radius of $R_S/r = 95\%$.

For the case of Asteroid 25143 Itokawa, this analysis determined that by dividing the body into its subsequent, homogeneous density regions, the "true" gravitational potential and acceleration field could be more accurately modeled. It was seen in the mascon derived orbits about Itokawa that accounting for the body's variable density does make a significant impact on the output trajectory. Therefore, the gravity model used to model small bodies for mission planning and scientific purposes must be able to accurately account for the variable density.

The spherical harmonic model is an elegant method for modeling the gravity field of small, asymmetric bodies with either homogeneous or variable densities. It was shown that a wide variety of objects can be handled by this modeling technique and the model can take into account the variable density nature of comets and asteroids. The coupling of the spherical harmonic model with the mascon distribution model adds to the accuracy of the final rendition of a given body; the higher the accuracy in the base model, the higher the accuracy of the series expansion. There are consequences to the mathematical rigor of this model though. As the spacecraft trajectory moves within the Brillouin sphere boundary, or on the boundary, the series expansion of the gravity field will diverge quickly from the true solution. This means that close proximity or landing operations will either need a different model or a variation of this model in order to properly enact the maneuver. It was also found that the "true" gravity and acceleration fields cannot be exactly recreated with a reasonable number of terms in the spherical harmonic series. As with any model, there will be some sort of deviation from the true solution and the differences will have to be accounted for in processes reliant upon that model. The spherical harmonic model presented does offer a reasonable deviation from the expected gravity and acceleration field in which a spacecraft operating on this model would not run into problems.

With the surplus of gravity models that are available for mission design teams and scientists to use, a model that is capable of being coupled with any other model is a strong asset. The spherical harmonic model presented offers this and has room for further innovation. This thesis quantified and defined the scope of this model and presented its ability to handle variable density bodies with high accuracy.

Some future adaptations and logical extensions of this model are:

“Dynamic” Brillouin Sphere Radius The current model uses a single radius Brillouin sphere who’s size is chosen based upon the altitude of a given orbit. This is dependent upon a circular orbit so that the trajectory does not enter the boundary of the sphere. Once elliptical trajectories are implemented, the Brillouin sphere radius may have to be automatically varied within the simulation where a smaller radius sphere is used when the spacecraft is a periapsis and a larger sphere is used when the craft is at apoapsis.

Coupling the Harmonic and Mascon Model All simulated trajectories must remain outside of the Brillouin sphere boundary because the series expansion only converges outside of this boundary. Within the Brillouin sphere, the mascon model governs the motion of the spacecraft. Realistically, the spacecraft will want to travel in close-proximity to the asteroid or comet’s surface, so if a dynamic Brillouin sphere radius is not implemented in the simulation, a binary model that switches between the spherical harmonic model outside of the Brillouin sphere and the mason model within the sphere will have to be used.

Bibliography

[1] ESO. The anatomy of an asteroid, 2014.

[2] J. C. Granahan, F. P. Fanale, M. S. Robinson, R. W. Carlson, L. W. Kamp, K. P. Klaasen, P. R. Weissman, M. Belton, D. Cook, K. Edwards, A. S. McEwen, L. A. Soderblom, B. T. Carcich, P. Helfenstein, D. Simonelli, P. C. Thomas, and J. Veverka. A Galileo Multi-Instrument Spectral Analysis of 951 Gaspra. In *Lunar and Planetary Science Conference*, volume 25 of *Lunar and Planetary Inst. Technical Report*, page 453, March 1994.

[3] L. A. D'Amario, L. E. Bright, and A. A. Wolf. Galileo trajectory design. , 60:23–78, May 1992.

[4] J. I. Trombka, L. R. Nittler, R. D. Starr, L. G. Evans, T. J. Mccoy, W. V. Boynton, T. H. Burbine, J. BrĂźckner, P. Gorenstein, S. W. Squyres, R. C. Reedy, J. O. Goldsten, L. Lim, K. Hurley, P. E. Clark, S. R. Floyd, T. P. Mcclanahan, E. Mccartney, J. Branscomb, J. S. Bhangoo, I. Mikheeva, and M. E. Murphy. The near-shoemaker x-ray/gamma-ray spectrometer experiment: Overview and lessons learned. *Meteoritics Planetary Science*, 36(12):1605–1616, 2001.

[5] P. Tsou, D. E. Brownlee, S. A. Sandford, F. Hörz, and M. E. Zolensky. Wild 2 and interstellar sample collection and Earth return. *Journal of Geophysical Research (Planets)*, 108:8113, October 2003.

[6] D. J. Scheeres, R. Gaskell, S. Abe, O. Barnouin-Jha, T. Hashimoto, J. Kawaguchi, J. Saito, M. Yoshikawa, N. Hirata, T. Mukai, M. Ishiguro, T. Kominato, K. Shirakawa, and M. Uo. The *Actual* dynamical environment about itokawa. *AIAA/AAS Astrodynamics Specialist Conference and Exhibit*, (AIAA 2006-6661), 2006.

[7] K.-H. Glassmeier, H. Boehnhardt, D. Koschny, E. Kührt, and I. Richter. The Rosetta Mission: Flying Towards the Origin of the Solar System. , 128:1–21, February 2007.

[8] D. K. Yeomans, S. R. Chesley, and N. Mastrodemos. Deep Impact: Effecting a spacecraft/comet collision at 10 km/sec. In *AAS/Division of Dynamical Astronomy Meeting #36*, volume 37 of *Bulletin of the American Astronomical Society*, page 533, May 2005.

[9] M. D. Rayman, T. C. Fraschetti, C. A. Raymond, and C. T. Russell. Dawn: A mission in development for exploration of main belt asteroids Vesta and Ceres. *Acta Astronautica*, 58:605–616, June 2006.

[10] T. G. Müller, J. Ďurech, M. Ishiguro, M. Mueller, T. Krühler, H. Yang, M.-J. Kim, L. O'Rourke, F. Usui, C. Kiss, B. Altieri, B. Carry, Y.-J. Choi, M. Delbo, J. P. Emery, J. Greiner, S. Hasegawa, J. L. Hora, F. Knust, D. Kuroda, D. Osip, A. Rau, A. Rivkin, P. Schady, J. Thomas-Osip, D. Trilling, S. Urakawa, E. Vilenius, P. Weissman, and P. Zeidler. Hayabusa-2 Mission Target Asteroid 162173 Ryugu (1999 JU3): Searching for the Object's Spin-Axis Orientation. *ArXiv e-prints*, November 2016.

[11] D. Lauretta and B. Clark. The OSIRIS-REx Sample Return Mission from Asteroid Bennu. In *41st COSPAR Scientific Assembly*, volume 41 of *COSPAR Meeting*, July 2016.

[12] J. E. Howard, T. D. Wilkerson, and J. N. Cantrell. Orbital dynamics about a slowly rotating asteroid. , 29:94–1, April 2002.

[13] G. Balmino. Gravitational potential harmonics from the shape of an homogeneous body. *Celestial Mechanics and Dynamical Astronomy*, 60:331–364, November 1994.

[14] J. M. Pearl and D. L. Hitt. Asteroid gravitational models using mascons derived from polyhedral sources. *AIAA/AAS Astrodynamics Specialist Conference, SPACE Conferences and Exposition*, (AIAA 2016-5260), 2016.

[15] A. Compère, J. Frouard, and B. Carry. Approximation of the gravitational potential of a non-spherical object: application to binary and triple asteroid systems. In F. Arenou and D. Hestroffer, editors, *Orbital Couples: Pas de Deux in the Solar System and the Milky Way*, pages 109–112, May 2012.

[16] R. A. Werner and D. J. Scheeres. Exterior Gravitation of a Polyhedron Derived and Compared with Harmonic and Mascon Gravitation Representations of Asteroid 4769 Castalia. *Celestial Mechanics and Dynamical Astronomy*, 65:313–344, 1997.

[17] R. A. Werner. The gravitational potential of a homogeneous polyhedron or don't cut corners. *Celestial Mechanics and Dynamical Astronomy*, 59:253–278, July 1994.

[18] T. G. G. Chanut, S. Aljbaae, and V. Carruba. Mascon gravitation model using a shaped polyhedral source. , 450:3742–3749, July 2015.

[19] Y. Takahashi and D. J. Scheeres. Small body surface gravity fields via spherical harmonic expansions. *Celestial Mechanics and Dynamical Astronomy*, 119:169–206, June 2014.

[20] J. M. Pearl and D. L. Hitt. A Polyhedral Potential Approach for Educational Simulation of Spacecraft in Orbit about Comet 67P/ChuryumovâGerasimenko. *AAS Paper 15-655*, 2015.

[21] S. R. Wood, J. M. Pearl, and D. L. Hitt. Polyhedral Potential Models for Close Proximity Orbital Simulations about Small Celestial Objects. *AIAA 2016-0450*, 2016.

[22] George Johnston Allman. On the attraction of ellipsoids, with a new demonstration of clairaut's theorem, being an account of the late professor mac cullagh's lectures on those subjects. *The Transactions of the Royal Irish Academy*, 22:379–395, 1849.

[23] W.D. McClain and D.A. Vallado. *Fundamentals of Astrodynamics and Applications*. Space Technology Library. Springer Netherlands, 2001.

[24] Ta-Hsin Li and Gerald R. North. Aliasing effects and sampling theorems of spherical random fields when sampled on a finite grid. *Annals of the Institute of Statistical Mathematics*, 49(2):341–354, 1997.

[25] M. Wieczorek. Software shtools.

[26] S. C. Lowry, P. R. Weissman, S. R. Duddy, B. Rozitis, A. Fitzsimmons, S. F. Green, M. D. Hicks, C. Snodgrass, S. D. Wolters, S. R. Chesley, J. Pittichová, and P. van Oers. The internal structure of asteroid (25143) Itokawa as revealed by detection of YORP spin-up. , 562:A48, February 2014.

[27] M. Kaasalainen, T. Kwiatkowski, M. Abe, J. Piironen, T. Nakamura, Y. Ohba, B. Dermawan, T. Farnham, F. Colas, S. Lowry, P. Weissman, R. J. Whiteley, D. J. Tholen, S. M. Larson, M. Yoshikawa, I. Toth, and F. P. Velichko. CCD photometry and model of MUSES-C target (25143) 1998 SF36. , 405:L29–L32, July 2003.

[28] R. S. Park, R. A. Werner, and S. Bhaskaran. Estimating Small-Body Gravity Field from Shape Model and Navigation Data. *Journal of Guidance Control Dynamics*, 33:212–221, January 2010.

[29] S. Tardivel. The Limits of the Mascons Approximation of the Homogeneous Polyhedron. *AIAA Paper 2016-5261*, 2016.

APPENDIX A

MASCON DISTRIBUTION MODEL

In the mascon model, a finite set of point-masses is used to to discretize the asteroid's volume. Several methods for distributing these points exist, including gridded approaches [16, 28], packing methods [29], and the use of finite volume meshes [14, 18]. In the present study, the distribution technique proposed by Pearl & Hitt [14] is used, which utilizes unstructured finite volume meshes consisting of polyhedral elements to distribute mascons.

The generation process involves three steps: (1) A triangular surface mesh (Figure A.1a) is used to create a tetrahedral volume mesh (Figure A.1b) using a modified Delaunay algorithm, (2) A polyhedral volume mesh is created by calculating the dual of the tetrahedral volume mesh, and (3) The elements of the resulting polyhedral volume mesh are approximated as point-mass with mass equal to the volume of the corresponding element multiplied by the local density. An example polyhedral volume mesh generated from the tetrahedral volume mesh of Figure A.1b is presented in Figure A.2a and the resulting mascon distribution is shown in . For a more in-depth discussion of the process the reader is referred to Pearl & Hitt [14].

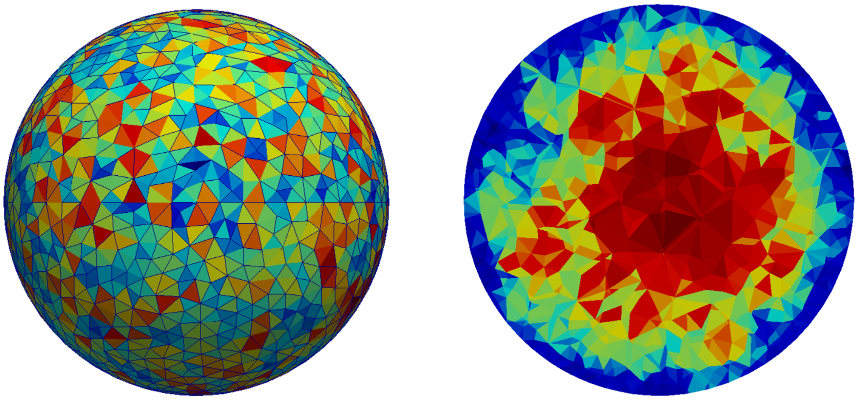

(a) Triangular Surface Mesh.

(b) Tetrahedral Volume Mesh.

Figure A.1: Tetrahedral Mesh of a Sphere Showing Graded Cells.

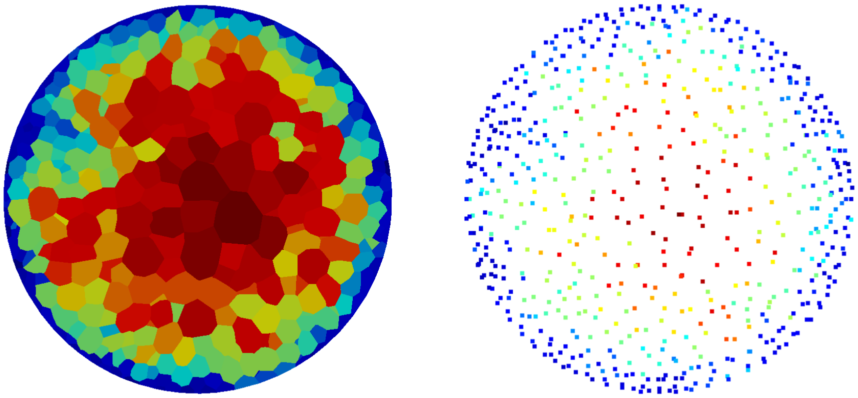

(a) Polyhedral-Dual Mesh.

(b) Mascon Distribution.

Figure A.2: Polyhedral-Dual Mesh of a Sphere and Resultant Mascons.

APPENDIX B

DERIVED SERIES COEFFICIENTS

ASTEROID 101955 BENNU

LO

$\mathbf{C}_n^m$

n\m	**0**	**1**	**2**	**3**	**4**
0	1.000458				
1	-4.7099×10^{-5}	-3.8472×10^{-5}			
2	-2.2403×10^{-3}	-7.9404×10^{-7}	3.8429×10^{-6}		
3	-2.2291×10^{-4}	8.1979×10^{-6}	-2.7339×10^{-7}	1.1855×10^{-5}	
4	$2.007\,42 \times 10^{-4}$	8.5982×10^{-7}	-1.4039×10^{-6}	-4.5443×10^{-8}	1.4219×10^{-5}

$\mathbf{S}_n^m$

n\m	**0**	**1**	**2**	**3**	**4**
0	0				
1	2.1329×10^{-4}				
2	1.2192×10^{-6}	1.0401×10^{-4}			
3	-6.8025×10^{-5}	4.7381×10^{-7}	6.8965×10^{-5}		
4	$1.178\,16 \times 10^{-6}$	-1.6582×10^{-5}	2.7901×10^{-7}	5.0729×10^{-5}	

MO

$\mathbf{C}_n^m$

n\m	**0**	**1**	**2**	**3**	**4**
0	1.0000110				
1	1.9985×10^{-6}	1.2794×10^{-5}			
2	-2.2705×10^{-4}	4.0042×10^{-7}	7.2919×10^{-5}		
3	-8.2952×10^{-6}	1.9371×10^{-6}	-2.6205×10^{-7}	3.3077×10^{-6}	
4	3.4462×10^{-6}	-7.6302×10^{-8}	-1.1601×10^{-6}	2.1603×10^{-7}	-1.4846×10^{-8}

$\mathbf{S}_n^m$

n\m	**0**	**1**	**2**	**3**	**4**
0	0				
1	-1.7396×10^{-7}				
2	2.8883×10^{-7}	-3.9857×10^{-6}			
3	2.2542×10^{-6}	-1.4170×10^{-7}	-1.3792×10^{-6}		
4	-2.7327×10^{-7}	2.0905×10^{-7}	5.1298×10^{-8}	4.8523×10^{-7}	